Journal of Glaciology

Article

Cite this article: Coffey NB, Lai C-Y (2025) Horizontal force-balance calving laws: Ice shelves, marine- and land-terminating glaciers. *Journal of Glaciology* **71**, e93, 1–23. https://doi.org/10.1017/jog.2025.10068

Received: 25 November 2024
Revised: 27 May 2025
Accepted: 6 June 2025

Keywords:
calving; crevasses; glacier mechanics

Corresponding author: Niall Bennet Coffey;
Email: nbcoffey@stanford.edu

© The Author(s), 2025. Published by Cambridge University Press on behalf of International Glaciological Society. This is an Open Access article, distributed under the terms of the Creative Commons Attribution-NonCommercial-ShareAlike licence (http://creativecommons.org/licenses/by-nc-sa/4.0), which permits non-commercial re-use, distribution, and reproduction in any medium, provided the same Creative Commons licence is used to distribute the re-used or adapted article and the original article is properly cited. The written permission of Cambridge University Press must be obtained prior to any commercial use.

Horizontal force-balance calving laws: Ice shelves, marine- and land-terminating glaciers

Niall Bennet Coffey and Ching-Yao Lai

Department of Geophysics, Stanford University, Stanford, CA, USA

Abstract

Predicting calving in glacier models is challenging, as observations of diverse calving styles appear to contradict a universal calving law. Here, we generalize and apply the analytical Horizontal Force-Balance fracture model from ice shelves to land- and marine-terminating glaciers. We consider different combinations of "crack configurations" including surface crevasses with or without meltwater above saltwater- or meltwater-filled basal crevasses. Our generalized crevasse-depth model analytically reveals that, in the absence of meltwater, the calving criterion depends on two dimensionless variables: buttressing B and dimensionless water level λ. Using a calving regime diagram, we quantitatively demonstrate that glaciers are generally more prone to calving with reduced buttressing B and lower water level λ. For a specified set of B, λ and crack configuration, an analytical calving law can be derived. For example, the calving law for an ice shelf, land-, or marine-terminating glacier with a dry surface crevasse above a saltwater basal crevasse reduces to a state with no buttressing ($B = 0$). With climate warming, glaciers are expected to become more vulnerable to calving due to meltwater-driven surface and basal crevassing. Our findings provide a framework for understanding diverse calving styles.

1. Introduction

Recent reviews of ice calving and stability (Alley and others, 2023; Bassis and others, 2024) elucidate how glacial retreat can transition across different calving regimes, e.g. from ice shelves to deep water glaciers to shallow water glaciers (Fig. 1). Assessing the impact of the marine ice cliff instability (MICI) (Bassis and Walker, 2012; Pollard and others, 2015; DeConto and Pollard, 2016) on sea level rise via ice sheet models is challenging due to the incomplete parametrization of calving rates (Morlighem and others, 2024) that are poorly constrained by observations. The recent Intergovernmental Panel on Climate Change assessment shows that MICI contributes to a highly uncertain high-end scenario, which can result in about one meter of global sea-level rise by 2100 (Pollard and others, 2015; DeConto and Pollard, 2016; Fox-Kemper and others, 2021).

Despite its importance, some of the most fundamental questions surrounding ice crevassing remain unanswered, including a predictive calving criterion. Various calving laws have been developed to model either the retreat rate (e.g. the von Mises law (Morlighem and others, 2016), eigencalving law (Levermann and others, 2012)) or position (e.g. the crevasse-depth law (Nye, 1955; Benn and others, 2007a; Nick and others, 2010)) of the calving front. Despite its wide use, it has been shown (Buck, 2023; Coffey and others, 2024) that in the Zero-Stress approximation (Nye, 1955; Benn and others, 2007a; Nick and others, 2010), the depth-integrated force at the crevassed and non-crevassed location are unbalanced. This has led to a modified crevasse-depth model for constant-thickness ice shelves (ISs) that satisfies Horizontal Force-Balance (HFB) (Buck, 2023). Importantly, HFB analytically predicts that the tensile stress required for calving is only half of that in the Zero-Stress approximation, which may substantially underestimate a glacier's vulnerability to calving. HFB provides reasonable agreement with observed ice shelf rift locations and yields a calving threshold that is insensitive to the vertical temperature profile (Coffey and others, 2024). Since analytical theories serve as foundational cases for developing physical understanding and benchmarking numerical methods that can simulate more complicated phenomena, it is crucial to develop physically self-consistent fracture models that can apply across diverse glacial environments, from ISs and marine-terminating glaciers (MTGs) to land-terminating glaciers (LTGs). This is the goal of the paper.

In this paper, we generalize the HFB approach of Buck (2023) and Coffey and others (2024) from constant-thickness ISs to land- and marine-terminating glaciers (Fig. 1). We consider six "crack configurations" involving different combinations of dry or meltwater surface and saltwater- or meltwater-filled basal crevasses (Fig. 3). Section 2 lays out the general formulation of HFB and the driving and resisting mechanisms for calving. Applying the general HFB formulation gives the analytical crack depths and calving criteria predictions for ISs, MTGs and

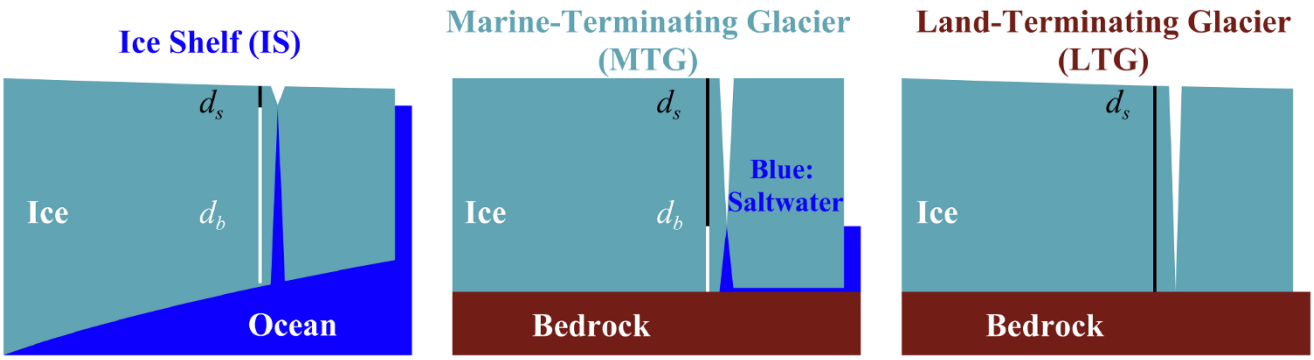

Figure 1. Schematic of the three cases considered in this paper: crevasses on an ice shelf, a marine-terminating glacier and a land-terminating glacier. Surface crevasses are considered in all three cases. Basal crevasse depth depends on whether it is filled with ocean saltwater or subglacial meltwater. Calving occurs when the surface crack and basal crack depths (d_s, d_b) fully occupy ice's thickness, $d_s + d_b = H$ which gives various calving laws derived in this paper.

LTGs in sections 2.1, 2.2 and 2.3, respectively. We hypothesize that the variety of observed calving styles may arise from different dominant balances in our force-balance equation, between sources of buttressing and drivers of calving, as discussed in section 3.

2. A force-balance framework (HFB) to predict crevasse depths

We begin this section by outlining the general steps to use the HFB approach to determine crevasse depths, depicted in Fig. 2. This approach is then applied to a variety of cases, from ISs (section 2.1, Fig. 5) to LTGs (section 2.2, Fig. 7) and MTGs (section 2.3, Fig. 2).

Assuming no acceleration, all of the forces F acting on a body must balance such that their sum is zero, $\Sigma F = 0$. This paper focuses on using the $\Sigma F = 0$ constraint to determine the crack depths and calving criteria.

The force balance $\Sigma F = 0$ can be expressed with a volume integral of the Stokes equation within a control volume V,

$$\iiint \left[\underline{\nabla} \cdot \underline{\underline{\sigma}} + \rho_i \underline{g}\right] dV = \underline{0}. \tag{1}$$

In (1), $\underline{\nabla}$ is the vector differential operator, $\underline{\underline{\sigma}}$ is the ice shelf Cauchy stress tensor, ρ_i is the ice density and $\underline{g}$ is the gravitational acceleration vector. Applying Gauss's theorem to (1), we obtain

$$\oiint \underline{\underline{\sigma}} \cdot \underline{n} dS + \iiint \rho_i \underline{g} dV = \underline{0}. \tag{2}$$

The horizontal component (perpendicular to gravity) of (2) per unit width (into the page) can be written in terms of the surface forces or traction $\underline{t} = \underline{\underline{\sigma}} \cdot \underline{n}$ (e.g. Malvern, 1969; Dahlen and Tromp, 1998; Rudnicki, 2014),

$$(\hat{\underline{x}}) : \oiint \hat{\underline{x}} \cdot \underline{\underline{\sigma}} \cdot \underline{n} dS = \oiint \hat{\underline{x}} \cdot \underline{t} dS = \Sigma F_x = 0. \tag{3}$$

This equation is the HFB per unit width. All that we need to know is the traction along the boundaries of our domain, or the sum of the forces acting on our body. This idea of integrating the momentum equation over a control volume is commonly used in many problems, such as with the Betti reciprocal relation (e.g. Dahlen and Tromp, 1998) and the Boundary Element Method (e.g. Crouch, 1976; Crouch and Starfield, 1983; Zarrinderakht and others, 2022). We use the glaciology convention (e.g. van der Veen and Whillans, 1989; Cuffey and Paterson, 2010) and define the resistive stress $\underline{\underline{R}}$ such that

$$\underline{\underline{\sigma}} = -p_I \underline{\underline{I}} + \underline{\underline{R}}, \tag{4}$$

or written in terms of the j, k components of the stress tensor, $\sigma_{jk} = -\delta_{jk} p_I + R_{jk}$, where $p_I \equiv \rho_i g(s - z)$ is the lithostatic pressure (scalar), δ_{jk} is the Kronecker delta function, s is the surface elevation and the vertical coordiante z is zero at the sea level, increasing upward.

We now consider two states: unfractured and fractured states (e.g. before and after crevassing). In the unfractured state, we may write (3) for a control volume delineated by the yellow dashed lines in Fig. 2 as

$$\int_{y_L}^{y_R} \int_b^s \hat{\underline{x}} \cdot \underline{\underline{\sigma}}^0 (x = x_c) \cdot \underline{n} dz dy = \overset{\text{Surface}}{\iint} \hat{\underline{x}} \cdot \underline{\underline{\sigma}}^0 \cdot \underline{n} dS + \overset{\text{Base}}{\iint} \hat{\underline{x}} \cdot \underline{\underline{\sigma}}^0 \cdot \underline{n} dS + \overset{\text{Front}}{\iint} \hat{\underline{x}} \cdot \underline{\underline{\sigma}}^0 \cdot \underline{n} dS + \overset{\text{Left}}{\iint} \hat{\underline{x}} \cdot \underline{\underline{\sigma}}^0 \cdot \underline{n} dS + \overset{\text{Right}}{\iint} \hat{\underline{x}} \cdot \underline{\underline{\sigma}}^0 \cdot \underline{n} dS, \tag{5}$$

where the superscript ^{0} denote the stress without crack formation. In the fractured state at $x = x_c$, the stresses at the cracked location differ from the unfractured state and (3) becomes

$$\int_{y_L}^{y_R} \int_b^s \hat{\underline{x}} \cdot \underline{\underline{\sigma}} (x = x_c) \cdot \underline{n} dz dy = \overset{\text{Surface}}{\iint} \hat{\underline{x}} \cdot \underline{\underline{\sigma}} \cdot \underline{n} dS + \overset{\text{Base}}{\iint} \hat{\underline{x}} \cdot \underline{\underline{\sigma}} \cdot \underline{n} dS + \overset{\text{Front}}{\iint} \hat{\underline{x}} \cdot \underline{\underline{\sigma}} \cdot \underline{n} dS + \overset{\text{Left}}{\iint} \hat{\underline{x}} \cdot \underline{\underline{\sigma}} \cdot \underline{n} dS + \overset{\text{Right}}{\iint} \hat{\underline{x}} \cdot \underline{\underline{\sigma}} \cdot \underline{n} dS. \tag{6}$$

Since the terms on the right-hand side of both equations are associated with horizontal forces acting on the control volume boundaries excluding the crevassing plane, which do not change between the fractured and the unfractured states, the right-hand sides of both equations are the same. Thus, with negligible vertical shear stress or approximately vertical cracks at $x = x_c$, the HFB for a control volume can be reduced to a local equation

$$\int_{y_L}^{y_R} \int_b^s \sigma_{xx}^0 (x = x_c) dz dy = \int_{y_L}^{y_R} \int_b^s \sigma_{xx} (x = x_c) dz dy. \tag{7}$$

https://doi.org/10.1017/jog.2025.10068 Published online by Cambridge University Press

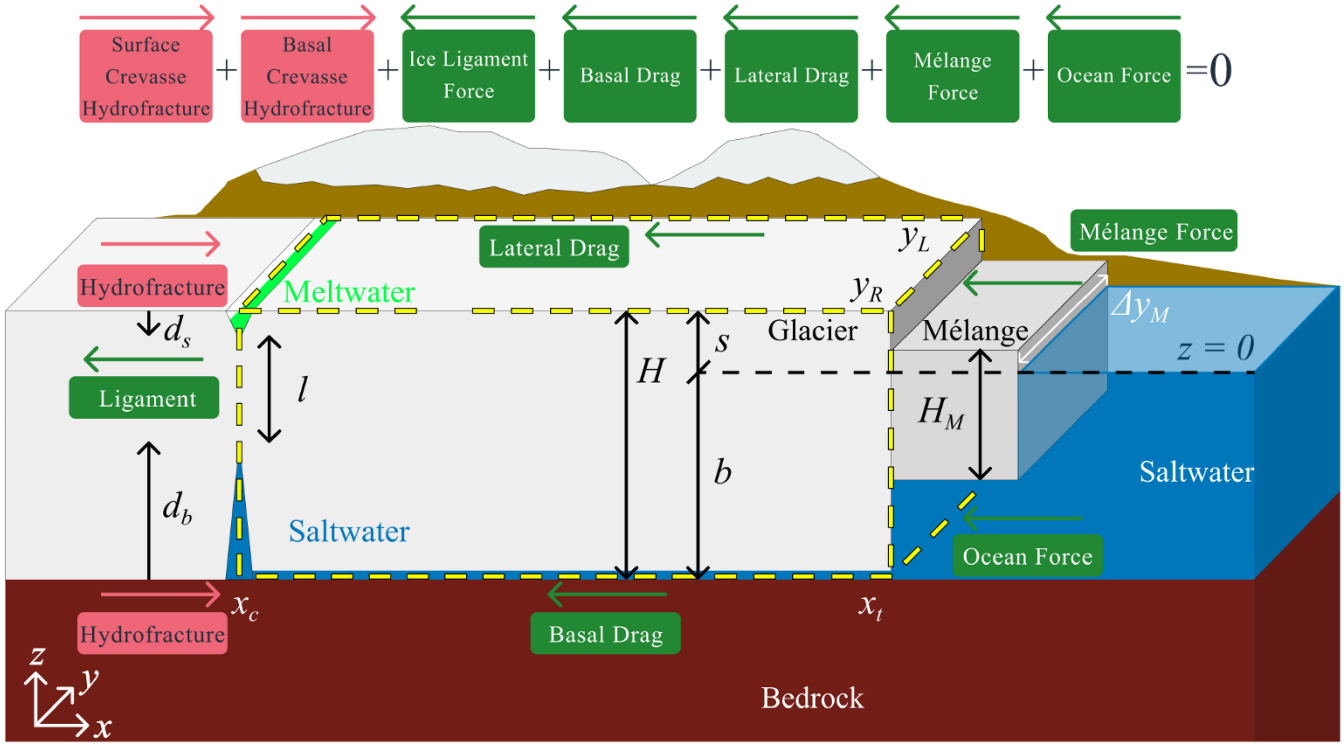

Figure 2. Schematic of the forces that drive calving (red) or inhibit calving (green), with force balance conceptualized atop the cartoon. See Table 1 for descriptions of symbols. Throughout this paper, saltwater and meltwater are shown in blue and light green, respectively.

For convenience, the stresses are width-averaged in the rest of the paper. The local HFB equation thus becomes

$$\int_b^s \sigma_{xx}^0 (x = x_c)\, dz = \int_b^s \sigma_{xx} (x = x_c)\, dz. \tag{8}$$

The HFBs in (3) and (8) applied to glacier crevassing have been extensively discussed in Buck (2023) and Coffey and others (2024). In this paper, we will use the local force balance (8) for each case considered in Fig. 1, from ISs through MTGs to LTGs.

Figure 2 shows an example of the forces acting on a control volume aligned with tensile, vertical crevasses on a MTG that can be described with (3). The driver of calving (red arrows) in our static framework is the hydrostatic water pressure in surface and basal crevasses. The forces that inhibit calving (green arrows), via reducing the tensile glaciological stresses around the crevasses and introducing buttressing, are basal drag (Vallot and others, 2018), lateral drag (Dupont and Alley, 2005), sea ice or ice mélange force (Amundson and others, 2010; Meng and others, 2025), the ice ligament force beneath the surface crevasse (Buck, 2023; Coffey and others, 2024) and the hydrostatic force from the ocean imposed at the calving front.

It will be shown that the outcome of the crack depths and calving criteria will depend on the net buttressing

$$B(x,t) = B_{Mélange}(t) + B_{Drags}(x). \tag{9}$$

$B_{Mélange}$ and B_{Drags} result from mélange and lateral or basal drag forces, respectively, which contribute positively to buttressing. In practice, it could be challenging to quantify each term in (9) due to the poorly known functional forms of these buttressing forces (see section 2.4). However, buttressing can be calculated if the glacial stress states are known. Ice shelf buttressing can be quantified using a similar line integral to (3) (Sergienko, 2025). For our modeling convenience we define the local dimensionless buttressing $B(x)$ (see Appendix D for more details) as

$$B \equiv 1 - \frac{\overline{R}_{xx}^0}{\overline{R}_{xx}^{B=0}}, \tag{10}$$

where $\overline{R}_{xx}^0$ is the depth- and width-averaged resistive stress (defined in (4)) in the unfractured state (Buck and Lai, 2021) and $\overline{R}_{xx}^{B=0}$ is the depth- and width-averaged resistive force of a glacier with no buttressing ($B_{Mélange} = B_{Drags} = 0$), defined as

$$\overline{R}_{xx}^{B=0} \equiv \frac{1}{2}\left(1 - \frac{\rho_i}{\rho_w}\lambda^2\right)\rho_i g H, \tag{11}$$

where $\lambda \equiv -\frac{\rho_w}{\rho_i}\frac{b}{H}$ is the dimensionless water level relative to flotation $\rho_i H/\rho_w$, and b is the bed elevation relative to the sea level. For ISs $\lambda = 1$, and the buttressing definition in (10) converges to that of Gudmundsson (2013) at the grounding line. Each symbol in (11) is defined in Table 1 and Fig. 2. Thus, the horizontal force per unit width at $x = x_c$ in the unfractured state can be written in terms of B as

$$\int_b^s \sigma_{xx}^0 (x = x_c)\, dz \equiv H\overline{R}_{xx}^0 - \frac{1}{2}\rho_i g H^2 = (1 - B)\, H\overline{R}_{xx}^{B=0} - \frac{1}{2}\rho_i g H^2. \tag{12}$$

We will find after solving for crack depths that there is a range of B where cracks can exist, from crack formation B^F to calving B^*, such that crack-depth solutions are valid within these bounds $B^* \le B \le B^F$.

To solve for only the surface crack depth, the force balance (8) is sufficient, since it yields an explicit relationship between crack

https://doi.org/10.1017/jog.2025.10068 Published online by Cambridge University Press

Table 1. Mathematical Symbols Glossary

Symbol	Definition	Value	Units
$b\,(x)$	Ice Base Elevation (relative to the sea level)	$[s-H, 0]$	m
B	Dimensionless Buttressing Number	Variable	1
B^*	Calving Threshold	Variable	1
B^F	Crack Formation Threshold	Variable	1
$\tilde{D}$	Dimensionless Total Crack Depth	$\tilde{d}_s + \tilde{d}_b$	1
d^{HFB}, d^{ZS}	Crack Depth: HFB or Zero-Stress	Variable	m
d_b	Basal Crack Depth	$[0, H-d_s]$	m
d_s	Surface Crack Depth	$[0, H-d_b]$	m
$\tilde{d}_{s,b}$, $\tilde{h}_w$, $\tilde{z}_h$	Dimensionless Crack Depths, Meltwater Depth, Head Height	$d_{s,b}/H, h_w/H, z_h/H$	1
$\underline{g}$, $-g\underline{\hat{z}}$	Gravitational Acceleration Vector	$-9.8\underline{\hat{z}}$	m s^{-2}
$H\,(x)$	Ice Thickness	Variable	m
H_M	Ice Mélange Thickness	$[0, H]$	m
h_w	Surface Meltwater Depth	$[0, d_s]$	m
$\underline{\underline{I}}$	Identity Tensor	$\mathrm{diag}(1,1,1)$	1
l	Ice Ligament Length	$[0, H-d_s-d_b]$	m
L	Ice Length	$x_t - x_c$	m
λ	Dimensionless Water Level	$-\rho_w b/\left(\rho_i H\right)$	1
$\underline{n}$	Outwards-Pointing Unit Normal Vector	Vector of length 1	1
$\underline{\nabla}$	Differential Operator	$\underline{\hat{x}}\partial_x + \underline{\hat{y}}\partial_y + \underline{\hat{z}}\partial_z$	m^{-1}
p	Pressure, i.e. the Isotropic Component of $\underline{\underline{\sigma}}$	-tr$\left(\underline{\underline{\sigma}}\right)/3$	Pa
p_l	Lithostatic Pressure	$\rho_i g\,(s\,(x)-z)$	Pa
$\underline{\underline{R}}$	Resistive Stress Tensor	$\underline{\underline{\sigma}} + p_l\underline{\underline{I}}$	Pa
ρ_i, ρ_m, ρ_w	Ice, Meltwater, Saltwater Density	917, 1000, 1028	kg m^{-3}
$s\,(x)$	Ice Surface Elevation (relative to the sea level)	$[0, H+b]$	m
$\underline{\underline{\sigma}}$	Cauchy Stress Tensor	Variable	Pa
$\underline{\underline{\tau}}$	Deviatoric Stress Tensor	$\underline{\underline{\sigma}} + p\underline{\underline{I}}$	Pa
x, y, z	Down Glacier, Across Glacier, Vertical	Coordinates	m
x_c, x_t, y_R, y_L	Crack Location, Ice Front, Right & Left Boundary	Variable	m
Δy, Δy_M	Glacier Width, Mélange Width	Variable	m
z_h	Subglacial Water Head Height	$[0, H]$	m

depth, buttressing B and dimensionless water level λ, e.g. (57). To solve for dual crack depths (surface cracks atop basal cracks), both the force balance (8) and crevasse-depth relation (13), i.e. the explicit dependence of the basal crack depth d_b on the surface crack depth d_s, are needed; otherwise, the system is underdetermined. In this paper, we will solve for both surface and dual cracks, as we generalize the previous HFB model (Buck, 2023; Coffey and others, 2024; Slater and Wagner, 2025) to six "crack configurations" illustrated in Fig. 3, each with their relevant setting, i.e. IS, MTG and LTG. As discussed in Buck (2023), Coffey and others (2024), two conditions are used to determine the surface and basal crack-depth relation: first, stress is continuous at crack tips (Buck and Lai, 2021); second, the ice has zero material strength. In the case of a surface crevasse and a basal crevasse with constant ice and saltwater densities ρ_i and ρ_w, this yields a crack depth relation of the form

$$\tilde{d}_b = f\left(\tilde{d}_s, \rho_i, \rho_w, \ldots\right) \tag{13}$$

where the dimensionless basal and surface crack depths $\tilde{d}_b, \tilde{d}_s$ are defined as the basal and surface crevasse depths normalized by ice thickness, i.e. $\tilde{d}_{b,s} \equiv d_{b,s}/H$. An example of (13) is (17). Solving (8) and (13) analytically yields simple expressions for tensile crevasse-induced calving laws that can be used to predict calving in numerical ice sheet models. In summary, our recipe for solving for crack depths in this paper is to solve

(1) (8) for HFB, and
(2) (13), if there are dual crevasses, which is obtained in this paper with the assumptions of zero material strength (Nye, 1955; Jezek, 1984; Benn and others, 2007a; Nick and others, 2010; Buck, 2023; Coffey and others, 2024) and continuity of stress at crack tips (Buck and Lai, 2021). Finite ice strength can be added, but it is not within the scope of this paper.

In the Zero-Stress approximation, the HFB (8) is not satisfied (Buck, 2023; Coffey and others, 2024). (13) alone is used to solve for crack depths with a background stress state defined in the absence of fractures (Nye, 1955; Benn and others, 2007a). Figure 4 demonstrates the issue through an example with a prescribed buttressing $B = 1 - x/L$: the Zero-Stress approximation underpredicts the crevasse depths, resulting in the calving stress threshold under the Zero-Stress approximation being twice as large as that predicted by the HFB framework (8) (Buck, 2023; Coffey and others, 2024), for a dry surface crevasse and a saltwater basal crevasse. In this paper, we derive the HFB-crack depths of six plausible crack configurations in Fig. 3 for ISs through MTGs to LTGs.

2.1. Ice shelf

2.1.1. Dry surface crevasse atop a saltwater basal crevasse (DS+SB)

The simplest dual crack solution exists for a freely floating ice shelf, and was originally derived in Buck (2023). Here, we restate the derivation for completeness, and see in Appendix D that the solution with variable thickness and isostasy is the same. We begin by determining the stress state of the unbroken ice ligament, l, defined in Fig. 5. In an unfractured state, the stress in the unbroken ligament is $\sigma_{xx} = -\rho_i g(s-z) + R_{xx}$. In a fractured state, the

https://doi.org/10.1017/jog.2025.10068 Published online by Cambridge University Press

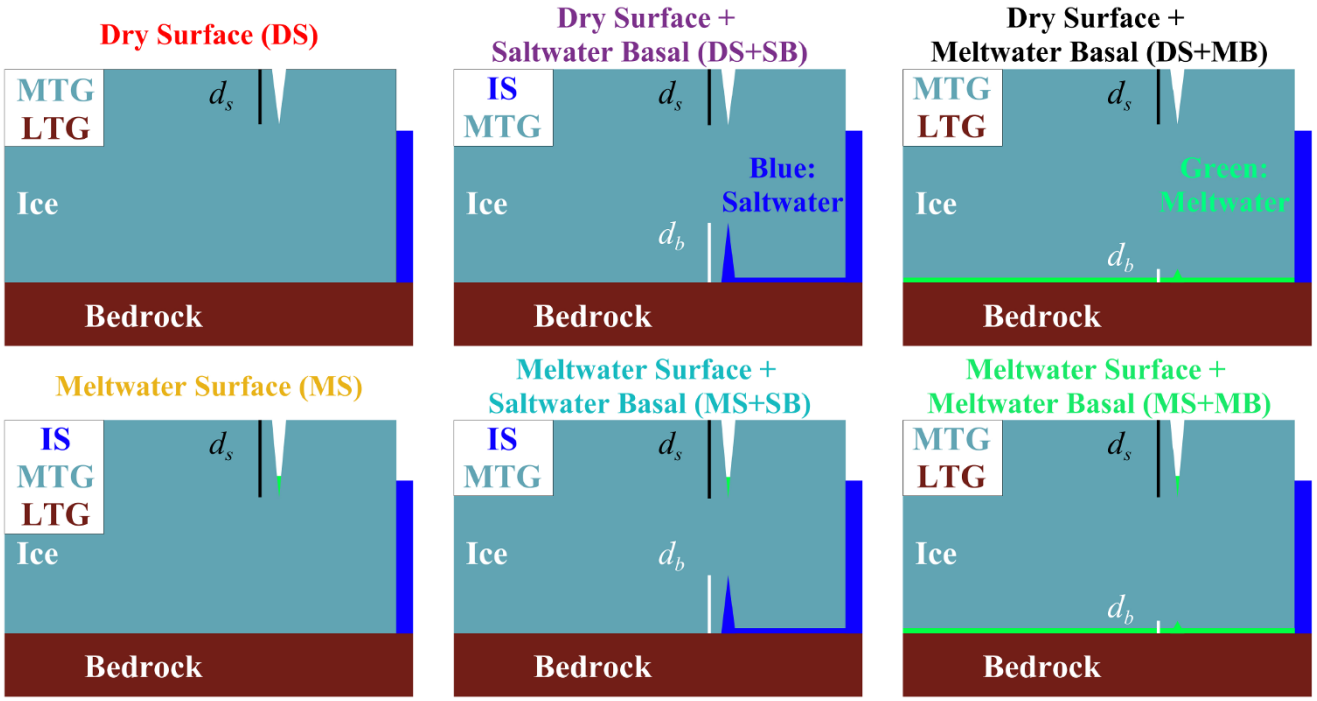

Figure 3. The six tensile crack configurations considered in this paper. The boxes in the top left corners of each case denote which of the three scenarios—IS, MTG, or LTG—is being considered. Throughout this paper, saltwater and meltwater are shown in blue and light green, respectively. The parameters used to generate these crack depths are $B = 0.1$, $\lambda = 0.75$, $\tilde{h}_w = 0.1$, $\tilde{z}_h = 0.7$.

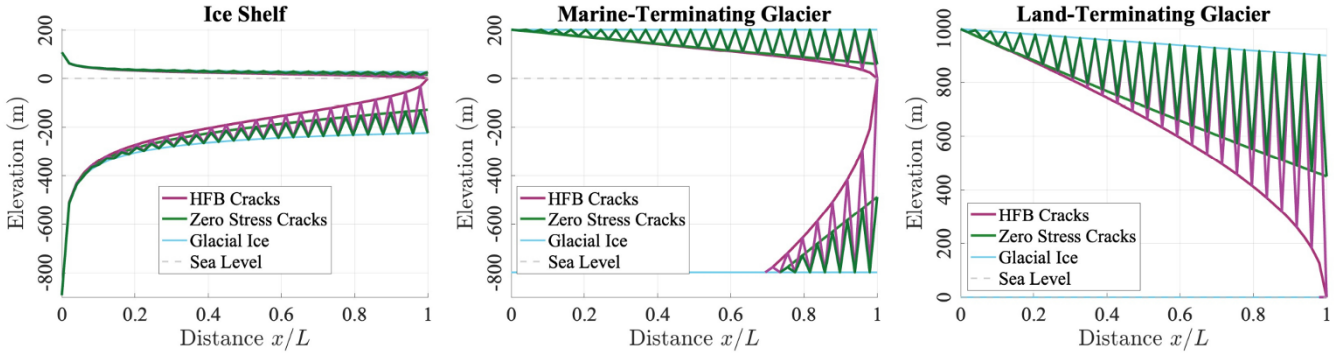

Figure 4. Comparing the crack depths predicted using the HFB and the Zero-Stress approximation for dry surface crevasses and saltwater basal crevasses (DS+SB) given an idealized dimensionless buttressing number of $B = 1 - x/L$. In HFB, crack depths are deeper than that predicted from the Zero-Stress approximation. Importantly, all HFB cases have calving occur at the ice front where $B = 0$, while the Zero-Stress approximation does not predict calving. According to HFB, instead of a critical stress criteria, zero buttressing $B = 0$ is the common calving criteria among the ice-shelf, marine-terminating and LTG cases (for a dry surface crevasse and potentially saltwater-filled basal crevasse in the absence of basal melting and material strength). The crack-depth envelopes are plotted as smooth curves, while the jaggedness is plotted to convey that these envelopes represent crack tip depth. Crack spacing is arbitrary in these plots.

longitudinal stress at the crevassed location $x = x_c$ satisfying the conditions of continuity of stress at the crack tips and zero material strength can be written in a piecewise expression (see derivation in Buck and Lai (2021); Buck (2023); Coffey and others (2024))

$$\sigma_{xx}(x_c, z) = \begin{cases} 0, & s - d_s \le z \le s \quad \text{(surface crevasse)} \\ -\rho_i g (s - z) + cR_{xx}, & b + d_b \le z \le s - d_s \quad \text{(unbroken ice ligament)} \\ \rho_w g z, & b \le z \le b + d_b \quad \text{(basal crevasse)} \end{cases} \tag{14}$$

Here, $cR_{xx}(x_c, z)$ parameterizes the sum of the crevasse-induced compressive stress in the unbroken ice ligament and $R_{xx} = 2\tau_{xx} + \tau_{yy}$ is the background resistive stress in the unfractured state (see Table 1 for definitions of resistive and deviatoric stresses). The constant c allows the stress in the unbroken ice ligament to update between the fractured and unfractured states, and will be determined shortly. Note that the Zero-Stress approximation corresponds to $c = 1$, i.e. not allowing the unbroken ice ligament stress state to differ between the unfractured and fractured ice states. For further discussion of cR_{xx} and the inconsistency of the Zero-Stress approximation, see section 2.3 and Appendix E of Coffey and others (2024). The continuity of stress between the crevasse and the unbroken ligament in (14) gives

$$-\rho_i g (s - (s - d_s)) + cR_{xx} = 0 \quad \text{at} \quad z(x_c) = s(x_c) - d_s \tag{15}$$

https://doi.org/10.1017/jog.2025.10068 Published online by Cambridge University Press

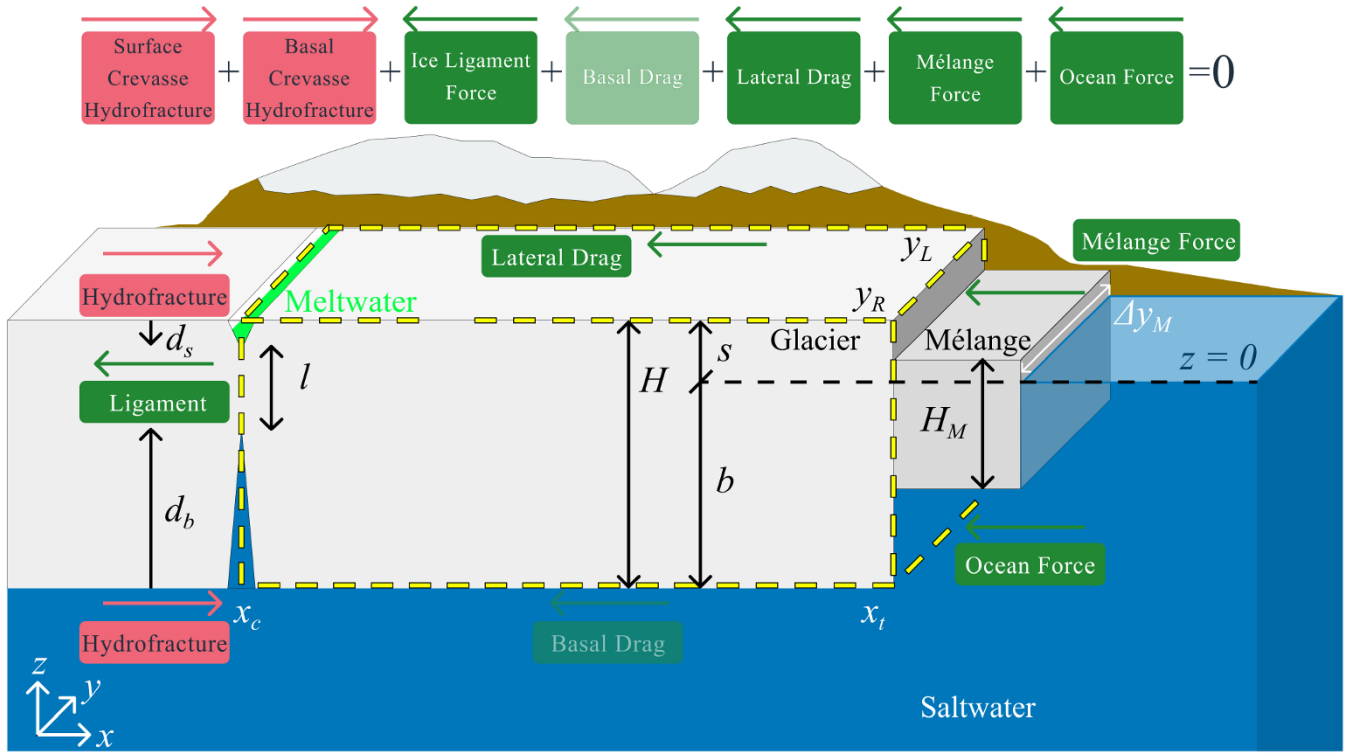

Figure 5. Equivalent version of Figure 2 for an ice shelf (IS) with meltwater in a surface crevasse and saltwater in a basal crevasse.

at the surface crack tip and

$$-\rho_i g\left(s-(b+d_b)\right)+cR_{xx}=\rho_w g\left(b+d_b\right) \text{ at } z\left(x_c\right)=b\left(x_c\right)+d_b \tag{16}$$

at the basal crack tip. The pair of (15) and (16) removes the unknown c and gives the following crack-depth relation (13), written in dimensionless form as

$$\tilde{d}_b=\tilde{d}_s\frac{\rho_i}{\rho_w-\rho_i}, \tag{17}$$

where $\tilde{d}\equiv d/H$ is the dimensionless crevasse depth and H is the ice thickness at $x=x_c$ in the unfractured state (Fig. 5). Note that this crevasse-depth relation (17) assumes isothermal ice. A vertically varying temperature profile would modify the crevasse relation as shown in Coffey and others (2024).

For an ice shelf, we write the HFB of (8) in its dimensionless form, normalized by $H\overline{R}^0_{xx}$, as

$$\frac{-\left(1-\tilde{d}_s-\tilde{d}_b\right)^2+\tilde{d}_b\frac{\rho_w}{\rho_i}\left(\tilde{d}_b-2\frac{\rho_i}{\rho_w}\right)}{1-\frac{\rho_i}{\rho_w}}=-B-\frac{\rho_i/\rho_w}{1-\frac{\rho_i}{\rho_w}}. \tag{18}$$

As in (8), the forces on the left-hand side and right-hand side represent the horizontal forces at $x=x_c$ in the fractured and unfractured ice states, respectively. Analytically solving (17) with (18), the crack-depth solutions for an ice shelf that is floating under Archimedean buoyancy everywhere are

$$\text{Surface crack depth:}\quad \tilde{d}_s=\left(1-\frac{\rho_i}{\rho_w}\right)\left(1-\sqrt{B}\right), \tag{19}$$

$$\text{Basal crack depth:}\quad \tilde{d}_b=\frac{\rho_i}{\rho_w}\left(1-\sqrt{B}\right). \tag{20}$$

We plot these crack depths in Fig. 6a,b. The total fraction of ice that is fractured, $\tilde{D}$, can be written in terms of B,

$$\tilde{D}\equiv\tilde{d}_s+\tilde{d}_b=1-\sqrt{B}. \tag{21}$$

These algebraic equations provide several insights. First, calving of a varying thickness ice shelf occurs ($\tilde{D}=1$) if there is no buttressing, setting the lower bound on buttressing B^* as

$$B^*=0, \tag{22}$$

which is the same calving criterion as that for constant thickness ISs as reported in (Buck, 2023; Coffey and others, 2024).

Second, the upper bound of buttressing B^F for there to be no fractures (fractures of zero depth) and thus no tension at the ice surface is

$$B^F=1. \tag{23}$$

Thus, for isostatic ISs with varying thicknesses, the nondimensional buttressing (9) must be $0\le B\le 1$ to permit the formation of dry surface crevasses and saltwater-filled basal crevasses. The calving criterion is $B=0$, as shown by the crack depths in Figs. 6a and 4. Throughout this paper, the lower bound of buttressing B^* occurs when crack(s) penetrate the entire ice thickness ($\tilde{D}=1$), and thus is our calving criteria. In general, there will be bounds on the amount of buttressing from full thickness fracture to no fracture, $B^*\le B\le B^F$, summarized along with crack-depth formulas in Tables 2, 3 and 4.

According to our HFB model, unbuttressed ISs with $B\left(x\right)=0$, i.e. ice tongues, are vulnerable to calving as the predicted surface and basal crevasses meet at the sea level everywhere (Fig. 6a). The existence of un-calved ice tongues can be attributable to non-zero material strength (e.g. Wells-Moran and others (2025)), non-zero buttressing such as sea ice (Christie and others, 2022; Gomez-Fell

https://doi.org/10.1017/jog.2025.10068 Published online by Cambridge University Press

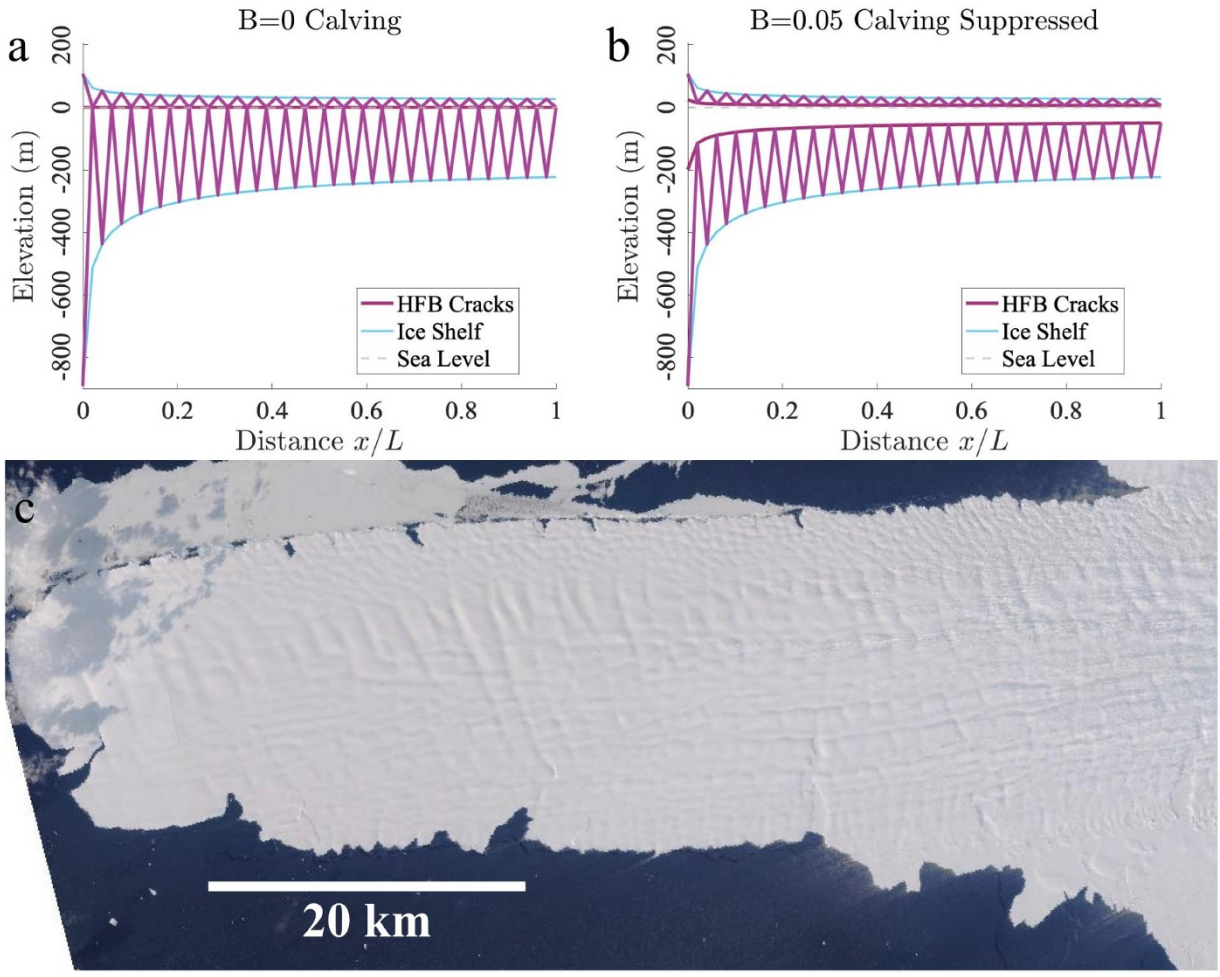

Figure 6. Ice tongues do not form with HFB unless there is a non-zero material strength, positive mass balance, or non-zero buttressing. We demonstrate the case of buttressing with the HFB solutions of (19) and (20) with zero buttressing in panel a and small buttressing in panel b. The ice thickness profile is the analytical solution of Van der Veen 1986. Crack spacing is arbitrary in these plots. Panel c shows the EPSG:3031 projection of the Drygalski Ice Tongue, Scott Coast, East Antarctica from Sentinel-2 on 7 March 2020 with Highlight Optimized Natural Color from the European Space Agency. Long, bright and dark shadow surface features perpendicular to flow may represent surface depressions atop basal crevasses (Luckman and others, 2012).

and others, 2022), and a positive mass balance (Bassis and Ma, 2015; Lawrence and others, 2023). This version of HFB does not consider more complicated 3D effects such as basal melt channels and their associated ice shelf flexure (Indrigo and others, 2021) or suture zones (Khazendar and others, 2011; Jansen and others, 2013; Kulessa and others, 2014; McGrath and others, 2014).

In the following sections, we apply the same procedure to obtain crevasse depths and calving criteria for various crack configurations.

2.1.2. Meltwater-containing surface crevasse atop a saltwater basal crevasse (MS+SB)

In warmer regions, meltwater on the ice shelf surface can enter into surface crevasses and has been implicated in the breakup of ISs. Here, we extend the HFB framework to consider surface crevasse deepening via hydrofracture (Scambos and others, 2009); the effects of surface loading of a lake on the ice shelf surface as in Banwell and others (2013), MacAyeal and Sergienko (2013) are left for future research.

The first difference between a meltwater-containing surface crevasse from the previous dry surface crevasse model is the crack-depth relation of (17), since this must now depend on the meltwater depth h_w in the surface crevasse. The stress profile at x_c in the fractured state also differs from (14) due to meltwater in the surface crevasse,

$$\sigma_{xx}(x_c, z) = \begin{cases} 0, & s - d_s + h_w \le z \le s \quad \text{(air in surface crevasse)} \\ -\rho_m g\,(s - d_s + h_w - z)\,, & s - d_s \le z \le s - d_s + h_w \quad \text{(meltwater in surface crevasse)} \\ -\rho_i g\,(s - z) + cR_{xx}, & b + d_b \le z \le s - d_s \quad \text{(unbroken ice ligament)} \\ \rho_w g z, & b \le z \le b + d_b \quad \text{(basal crevasse)} \end{cases} \tag{24}$$

At the surface crevasse tip $z = s - d_s$, we have

$$-\rho_m g\,(s - d_s + h_w - (s - d_s)) = -\rho_i g\,(s - (s - d_s)) + cR_{xx}, \tag{25}$$

where ρ_m is the density of meltwater. Similarly, at the basal crevasse tip $z = b + d_b$, we have that

$$\rho_w g\,(b + d_b) = -\rho_i g\,(s - (b + d_b)) + cR_{xx}. \tag{26}$$

https://doi.org/10.1017/jog.2025.10068 Published online by Cambridge University Press

Combining (25) and (26) while noting that $s = \left(1 - \frac{\rho_i}{\rho_w}\right) H$ and $b = -\frac{\rho_i}{\rho_w} H$ for a freely floating ice shelf, we determine the crack-depth relation

$$\tilde{d}_s = \frac{\rho_m}{\rho_i}\tilde{h}_w + \left(\frac{\rho_w}{\rho_i} - 1\right)\tilde{d}_b, \quad \text{for} \quad 0 \le \tilde{h}_w \le \frac{\rho_i}{\rho_m}, \tag{27}$$

where $\tilde{h}_w \equiv h_w/H$ and its upper bound that permits a dual crack solution will be explained in (37). Note that when $\tilde{h}_w = 0$, (17) and (27) are the same.

Next, the force balance in (18) must change to account for the both the hydrostatic meltwater pressure in the surface crevasse and the subsequent change in the stress in the unbroken ligament, resulting in

$$\frac{-\frac{\rho_m}{\rho_i}\tilde{h}_w^2 - \left(1 - \tilde{d}_s - \tilde{d}_b\right)^2 - 2\frac{\rho_m}{\rho_i}\tilde{h}_w\left(1 - \tilde{d}_s - \tilde{d}_b\right) + \tilde{d}_b\frac{\rho_w}{\rho_i}\left(\tilde{d}_b - 2\frac{\rho_i}{\rho_w}\right)}{1 - \frac{\rho_i}{\rho_w}} = -B - \frac{\rho_i/\rho_w}{1 - \frac{\rho_i}{\rho_w}}. \tag{28}$$

In the limiting case of $\tilde{h}_w = 0$, (18) and (28) would be identical.

Solving (27) and (28), we find that

$$\text{Surface crack depth:} \quad \tilde{d}_s = \frac{\rho_m}{\rho_i}\tilde{h}_w + \left(1 - \frac{\rho_i}{\rho_w}\right)\left(1 - \sqrt{B + \frac{\rho_m - \rho_i}{\rho_w - \rho_i}\frac{\rho_m\rho_w}{\rho_i^2}\tilde{h}_w^2}\right) \quad \text{for} \quad 0 \le \tilde{h}_w \le \frac{\rho_i}{\rho_m}, \tag{29}$$

$$\text{Basal crack depth:} \quad \tilde{d}_b = \frac{\rho_i}{\rho_w}\left(1 - \sqrt{B + \frac{\rho_m - \rho_i}{\rho_w - \rho_i}\frac{\rho_m\rho_w}{\rho_i^2}\tilde{h}_w^2}\right) \quad \text{for} \quad 0 \le \tilde{h}_w \le \frac{\rho_i}{\rho_m}. \tag{30}$$

We now construct bounds for buttressing $B^* \le B \le B^F$ as before. The minimum stress or maximum buttressing to permit basal crack formation is

$$B^F = 1 - \frac{\rho_m - \rho_i}{\rho_w - \rho_i}\frac{\rho_m\rho_w}{\rho_i^2}\tilde{h}_w^2 \quad \text{for} \quad 0 \le \tilde{h}_w \le \frac{\rho_i}{\rho_m}. \tag{31}$$

Summing (29) and (30) gives

$$\tilde{D} = \frac{\rho_m}{\rho_i}\tilde{h}_w + 1 - \sqrt{B + \frac{\rho_m - \rho_i}{\rho_w - \rho_i}\frac{\rho_m\rho_w}{\rho_i^2}\tilde{h}_w^2}, \tag{32}$$

thus calving or $\tilde{D} = 1$ occurs when

$$B^* = \frac{\rho_w - \rho_m}{\rho_w - \rho_i}\frac{\rho_m}{\rho_i}\tilde{h}_w^2 \quad \text{for} \quad 0 \le \tilde{h}_w \le \frac{\rho_i}{\rho_m}. \tag{33}$$

Comparing (33) with (22), we see that adding meltwater allows calving to occur in buttressed regions of the ice shelf. Comparing (31) with (33), we see that B^F decreases with $\tilde{h}_w^2$, whereas B^* increases with $\tilde{h}_w^2$. This buttressing range $B^* \le B \le B^F$ permits the dual crack configuration to still obey the force balance constraint. Continuously adding surface meltwater $\tilde{h}_w$ will either cause calving or provide enough pressure to close the basal crevasse. In the latter case, $B^F \le B^*$, and a transition to a new crack configuration, i.e. a meltwater-containing surface crevasse without a basal crevasse (MS), must occur. By adding meltwater to highly buttressed ice shelf regions, calving is reached by a meltwater-containing surface crevasse alone.

2.1.3. Meltwater-containing surface crevasse without a basal crevasse (MS)

As in the previous section, the stress balance at the surface crevasse tip (25) is identical, but there is no basal crevasse and thus no need for (26). The force-balance equation

$$\frac{-\frac{\rho_m}{\rho_i}\tilde{h}_w^2 - \left(1 - \tilde{d}_s\right)^2 - 2\frac{\rho_m}{\rho_i}\tilde{h}_w\left(1 - \tilde{d}_s\right)}{1 - \frac{\rho_i}{\rho_w}} = -B - \frac{\rho_i/\rho_w}{1 - \frac{\rho_i}{\rho_w}} \tag{34}$$

differs from (28) in that the basal crevasse does not exist $\tilde{d}_b = 0$. The analytical solution to (34) is

$$\text{Surface crack depth:} \quad \tilde{d}_s = 1 + \frac{\rho_m}{\rho_i}\tilde{h}_w - \sqrt{B\left(1 - \frac{\rho_i}{\rho_w}\right) + \frac{\rho_i}{\rho_w} + \frac{\rho_m}{\rho_i}\left(\frac{\rho_m}{\rho_i} - 1\right)\tilde{h}_w^2} \quad \text{for} \quad \frac{\rho_i}{\rho_m} \le \tilde{h}_w \le 1. \tag{35}$$

Calving occurs when $\tilde{d}_s = 1$, and we may substitute this into (35) to solve for the calving threshold,

$$B^* = \frac{-\frac{\rho_i}{\rho_w} + \frac{\rho_m}{\rho_i}\tilde{h}_w^2}{1 - \frac{\rho_i}{\rho_w}} \quad \text{for} \quad \frac{\rho_i}{\rho_m} \le \tilde{h}_w \le 1. \tag{36}$$

Calving is possible at higher levels of buttressing due to larger amounts of meltwater $\tilde{h}_w$. To determine the transition from dual crevasses to a meltwater-containing surface crevasse without a basal crevasse (MS), we must set (31) and (33) equal to solve for meltwater depth $\tilde{h}_w^T$ at the limit of $B^* = B^F$. This gives the buttressing B^T and water depth $\tilde{h}_w^T$ at the transition from calving by dual crevasses to calving by a meltwater-containing surface crevasse.

$$B^T = \frac{\frac{\rho_w}{\rho_m} - 1}{\frac{\rho_w}{\rho_i} - 1}, \quad \text{and} \quad \tilde{h}_w^T = \frac{\rho_i}{\rho_m}. \tag{37}$$

Thus, in HFB, the meltwater-containing surface crevasse without a basal crevasse (MS) case on an ice shelf exists for $B^T \le B^* \le B$, defined in (37) and (36). For calving to occur, the lowest amount of meltwater in this configuration is $\tilde{h}_w^T = \rho_i/\rho_m \approx 0.917$, showing that more than 90% of the ice thickness must be filled with meltwater in a surface crevasse to cause calving from a meltwater-containing surface crevasse without a basal crevasse (MS) on an ice shelf. This is consistent with the previously reported results using Linear Elastic Fracture Mechanics (LEFM) (Lai and others, 2020).

2.2. Land-terminating glacier

LTGs are defined here in the absence of water at the ice front (Figs. 1 and 7). As such, no saltwater basal crevasses can form. Note that in reality, LTGs often terminate in a toe or snout instead of an idealized vertical cliff as in Fig. 7. Additionally, basal crevasses on LTGs forced by basal meltwater is a hypothetical scenario and may be challenging to observe. However, the derivation of these hypothetical cases in this subsection offers a useful theoretical comparison with MTGs, which we explore in the next subsection. Specifically, assuming a flat bed and constant thickness, the LTG is equivalent

https://doi.org/10.1017/jog.2025.10068 Published online by Cambridge University Press

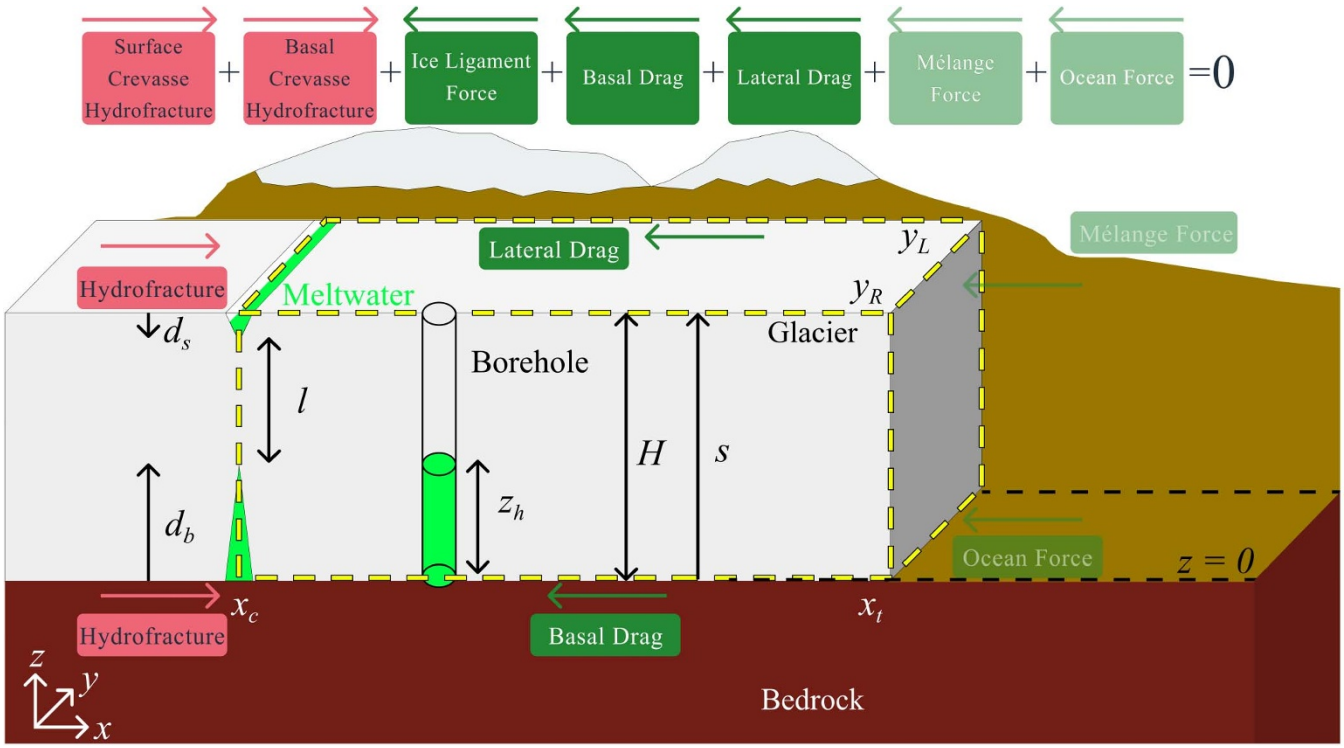

Figure 7. Equivalent version of Figure 2 for an LTG with meltwater in crevasses. The ocean force and floating ice mélange are absent for an LTG.

to the MTG with $\lambda = 0$, and (11) becomes

$$\overline{R}_{xx}^{B=0}(\lambda = 0) = \frac{1}{2}\rho_i g H. \tag{38}$$

Distinct from the previous ice shelf cases, the scenarios considered for LTGs are dry surface crevasses (DS), meltwater-containing surface crevasses (MS) and a combination of either of those surface crevasses with a meltwater basal crevasse (DS+MB/MS+MB). We now elaborate on each case.

2.2.1. Dry surface crevasse without a basal crevasse (DS)

The case of a dry tensile surface crevasse on an LTG represents a simple starting point for considering stability to fracture. Since we do not have a basal crevasse, there is no relation between crack depths (13). Instead of having two equations, (13) and (8), with two unknowns, $\tilde{d}_b$ and $\tilde{d}_s$ given B, we have one equation (8) with one unknown $\tilde{d}_s$ given B.

As before, we use continuity of stress at the surface crevasse tip given the zero-strength assumption to solve for the stress state in the unbroken ice. At the surface crack tip $x = x_c, z(x_c) = s(x_c) - d_s$, the stress balance is

$$-\rho_i g\,(s - (s - d_s)) + cR_{xx} = 0. \tag{39}$$

Solving for the constant c gives the stress profile in the ice

$$\sigma_{xx}(x = x_c, z \le s - d_s) = -p_l + cR_{xx} = -\rho_i g\,(s - d_s - z). \tag{40}$$

Then we may write the force balance (8) in dimensional form as

$$-\frac{\rho_i g}{2}(H - d_s)^2 = (1 - B)\,H\overline{R}_{xx}^{B=0} - \frac{\rho_i g H^2}{2}. \tag{41}$$

(41) gives the nondimensional surface crevasse depth,

$$\text{Surface crack depth:}\quad \tilde{d}_s = 1 - \sqrt{B}. \tag{42}$$

Thus, for the surface crack to form,

$$B^F = 1, \tag{43}$$

and for calving, the buttressing is

$$B^* = 0. \tag{44}$$

This equation shows that for an LTG with zero material strength, a dry surface crevasse will reach the base of the glacier in the absence of any buttressing, e.g. no basal or lateral drag, $B = B^* = 0$ (shown in purple in Fig. 4 and in Fig. 9i). For there to be no cracks, i.e. $\tilde{d}_s = 0$, the buttressing must be $B = B^F = 1$. These B^*, B^F results are the same as the dual crack configuration for the IS in (21).

2.2.2. Meltwater-containing surface crevasse without a basal crevasse (MS)

The addition of meltwater in a surface crevasse changes both the stress in the unbroken ice ligament (40) and adds a water pressure term to the force balance in (41). To satisfy continuity of stress at the crack tip, the analogous equation to the dry surface crevasse case (39) is

$$-\rho_i g\,(s - (s - d_s)) + cR_{xx} = -\rho_m g h_w. \tag{45}$$

Thus, the stress in the ice below the surface crevasse, analogous to (40), is

$$\sigma_{xx}(x = x_c, z) = -\rho_i g\,(s - d_s - z) - \rho_m g h_w. \tag{46}$$

Similarly, the force-balance equation analogous to (41) now has two new terms from the water pressure and updated stress in the

https://doi.org/10.1017/jog.2025.10068 Published online by Cambridge University Press

unbroken ligament,

$$-\frac{\rho_i g}{2}(H-d_s)^2-\rho_m g h_w (H-d_s)-\frac{\rho_m g h_w^2}{2} = (1-B)\,H\overline{R}_{xx}^{B=0}-\frac{\rho_i g H^2}{2}. \quad (47)$$

This quadratic equation can be simplified and solved for the dimensionless crack depth $\tilde{d}_s$,

$$\text{Surface crack depth:}\quad \tilde{d}_s = 1+\frac{\rho_m}{\rho_i}\tilde{h}_w - \sqrt{B+\frac{\rho_m}{\rho_i}\left(\frac{\rho_m}{\rho_i}-1\right)\tilde{h}_w^2}\quad \text{for}\quad 0\le \tilde{h}_w \le 1. \quad (48)$$

In the absence of meltwater or $\tilde{h}_w = 0$, this equation converges to the dry surface crevasse case (41). We now discuss the range of $B^* \le B \le B^F$ that permits this crack-depth solution.

First, the smallest crack depth in (48) is $\tilde{d}_s = \tilde{h}_w$. Using this equality, one can solve for the maximum buttressing that permits a meltwater hydrofracture,

$$B^F = 1+\left(\frac{\rho_m}{\rho_i}-1\right)\tilde{h}_w\left(2-\tilde{h}_w\right)\quad \text{for}\quad 0\le \tilde{h}_w \le 1. \quad (49)$$

When $\tilde{h}_w = 0$ this equation converges to the dry surface crevasse case. However, when there is meltwater $\tilde{h}_w > 0$, the buttressing upper bound is larger, indicating that hydrofracture is less stable than dry fracture.

Second, the case of calving is determined by setting $\tilde{d}_s = 1$ in (48),

$$B^* = \frac{\rho_m}{\rho_i}\tilde{h}_w^2 \quad \text{for}\quad 0\le \tilde{h}_w \le 1. \quad (50)$$

Unlike the dry surface crevasse case, calving due to a meltwater surface crevasse can now occur in buttressed regions $B > 0$. Ice becomes less stable with a larger density ratio ρ_m/ρ_i and with more meltwater $\tilde{h}_w \equiv h_w/H$.

2.2.3. Surface crevasse atop a meltwater basal crevasse (DS+MB/MS+MB)

As seen in the previous section, the solution for the dry surface crevasse on an LTG is a limiting case of the meltwater-containing surface crevasse when there is no meltwater, or $\tilde{h}_w = 0$. As such, we now derive the dual solution for a surface crevasse, dry or with meltwater and a basal crevasse filled with subglacial meltwater.

The stress in the unbroken ice ligament has the same form as (46). However, since we have two crevasses, we now seek a crack-depth relation as outlined in (13). Continuity of stress, as applied in (39) and (45) at the surface crevasse tip, is applied at the basal crack tip and gives the crack-depth relation

$$\tilde{d}_s = 1-\tilde{d}_b-\frac{\rho_m}{\rho_i}\left(\tilde{z}_h-\tilde{h}_w-\tilde{d}_b\right), \quad (51)$$

where $\tilde{z}_h \equiv z_h/H$ and z_h is the piezometric head height, i.e. the height to which the water would rise relative to the ice bed $z = b < 0$ in a borehole. Note that in dimensional form, the hydrostatic water pressure in the basal crevasse is set to be $-\rho_m g\,(b+z_h-z)$.

Next, we specify the HFB of (8). Relative to (47), there is an additional force due to the water pressure in the basal crevasse, and an adjustment to the ice pressure forces at $x = x_c$ because the ligament l is now smaller with dual cracks (see Fig. 7). Written in a nondimensional form, the HFB equation becomes

$$-\left(1-\tilde{d}_s-\tilde{d}_b\right)^2-2\frac{\rho_m}{\rho_i}\tilde{h}_w\left(1-\tilde{d}_s-\tilde{d}_b\right)-\frac{\rho_m}{\rho_i}\tilde{h}_w^2 -\frac{\rho_m}{\rho_i}\tilde{d}_b\left(2\tilde{z}_h-\tilde{d}_b\right) = -B. \quad (52)$$

With the crack-depth relation (51) and HFB (52), we analytically solve for crack-depth solutions,

$$\text{Surface crack depth:}\quad \tilde{d}_s = 1+\frac{\rho_m}{\rho_i}\tilde{h}_w-\tilde{z}_h - \sqrt{\left(1-\frac{\rho_i}{\rho_m}\right)\left[B-\frac{\rho_m}{\rho_i}\left(\tilde{z}_h^2-\left(\frac{\rho_m-\rho_i}{\rho_i}\right)\tilde{h}_w^2\right)\right]}\quad \text{for}\quad 0\le \tilde{h}_w \le \tilde{z}_h, \quad (53)$$

$$\text{Basal crack depth:}\quad \tilde{d}_b = \tilde{z}_h - \frac{\rho_i}{\rho_m}\sqrt{\frac{\rho_m}{\rho_m-\rho_i}\left[B-\frac{\rho_m}{\rho_i}\left(\tilde{z}_h^2-\left(\frac{\rho_m-\rho_i}{\rho_i}\right)\tilde{h}_w^2\right)\right]}\quad \text{for}\quad 0\le \tilde{h}_w \le \tilde{z}_h. \quad (54)$$

We next seek the buttressing range that permits crack formation, $B^* \le B \le B^F$. Unlike the case of MS without a basal crevasse (49), the smallest crack depth in this dual crack solution occurs when there is no basal crevasse, $\tilde{d}_b = 0$. Plugging this in to (54) gives

$$B^F = \frac{\rho_m}{\rho_i}\left(\frac{\rho_m}{\rho_i}\tilde{z}_h^2-\frac{\rho_m-\rho_i}{\rho_i}\tilde{h}_w^2\right)\quad \text{for}\quad 0\le \tilde{h}_w \le \tilde{z}_h. \quad (55)$$

The calving criterion can be determined from (53) and (54) with $\tilde{D} \equiv \tilde{d}_s+\tilde{d}_b = 1$,

$$B^* = \frac{\rho_m}{\rho_i}\tilde{z}_h^2 \quad \text{for}\quad 0\le \tilde{h}_w \le \tilde{z}_h. \quad (56)$$

Interestingly, the calving threshold for a meltwater-containing surface crevasse over a meltwater basal crevasse does not depend on the amount of water in the surface crevasse. However, the buttressing bounds $B^* \le B \le B^F$ require that $B^* \le B^F$: according to (56) and (55), this inequality holds on LTGs when $\tilde{z}_h \geqslant \tilde{h}_w$. Thus, calving is determined by the basal crevasse for the case of a meltwater-containing surface crevasse atop a meltwater basal crevasse, and this dual crack configuration is only valid when the head height of the meltwater is at least larger than the meltwater depth in the surface crevasse, $\tilde{z}_h \geqslant \tilde{h}_w$. However, if the meltwater basal crevasse closes because $\tilde{h}_w \geqslant \tilde{z}_h$, the calving threshold would be set by the meltwater-crevasse without a basal crevasse (MS) case defined in the previous section (50).

2.3. Marine-terminating glacier

MTGs cover the widest range of scenarios and have crack solutions converge to LTGs when the water at the ice front is zero. MTGs also have crack solutions converge to ISs when the basal crack is saltwater-filled and the ice is at flotation everywhere. Thus, this section contains the most generalized crack solutions that, under some limits, converge to the previously presented cases. Specifically, to maintain a consistent definition of buttressing between ISs, MTGs and LTGs, the MTG case considers constant thickness and flat bed slope (see Appendix D).

https://doi.org/10.1017/jog.2025.10068 Published online by Cambridge University Press

2.3.1. Dry surface crevasse without a basal crevasse (DS)

The force-balance equation is the similar to that of LTGs (41), but is now dependent on the dimensionless water level $\lambda \equiv \frac{\rho_w}{\rho_i}\frac{-b}{H} \geqslant 0$, which will be important throughout the MTG section,

$$-\frac{\rho_i g}{2}(H-d_s)^2 = (1-B)\,H\overline{R}_{xx}^{B=0} - \frac{\rho_i g H^2}{2}. \tag{57}$$

As before, we use ρ_w as the saltwater density, but it can be defined for alternative applications as the lake water density. (57) gives the surface crevasse depth,

$$\text{Surface crack depth:}\quad \tilde{d}_s = 1 - \sqrt{B\left(1-\frac{\rho_i}{\rho_w}\lambda^2\right) + \frac{\rho_i}{\rho_w}\lambda^2}. \tag{58}$$

This solution is shown by the red curve in Fig. A1 in Appendix A. A proglacial body of water alone acts to reduce the depth of cracks. For there to be no crevasse, we would have that

$$B^F = 1, \tag{59}$$

while calving would occur when

$$B^* = \frac{-\frac{\rho_i}{\rho_w}\lambda^2}{1-\frac{\rho_i}{\rho_w}\lambda^2}. \tag{60}$$

Thus, negative buttressing is needed for calving to occur via a dry surface crevasse in a MTG. According to (9), negative buttressing would not occur in our width-averaged framework.

2.3.2. Meltwater-containing surface crevasse without a basal crevasse (MS)

Following the corresponding section for an LTG, we extend the derivation to include proglacial water at the calving front. The stress in the ice ligament from the base to the surface crevasse tip has the same form as (46). The force balance (47) now has the slightly modified form,

$$\begin{aligned} &-\frac{\rho_i g}{2}(H-d_s)^2 - \rho_m g h_w (H-d_s) - \frac{\rho_m g h_w^2}{2} \\ &= (1-B)\,H\overline{R}_{xx}^{B=0} - \frac{\rho_i g H^2}{2}. \end{aligned} \tag{61}$$

The solution for surface crevasse depth then becomes

$$\begin{aligned} &\text{Surface crack depth:}\quad \tilde{d}_s = 1 + \frac{\rho_m}{\rho_i}\tilde{h}_w \\ &- \sqrt{B\left(1-\frac{\rho_i}{\rho_w}\lambda^2\right) + \frac{\rho_i}{\rho_w}\lambda^2 + \frac{\rho_m}{\rho_i}\left(\frac{\rho_m}{\rho_i}-1\right)\tilde{h}_w^2} \quad \text{for} \\ &0 \leq \tilde{h}_w \leq 1. \end{aligned} \tag{62}$$

To have the minimal meltwater-filled crack depth $\tilde{d}_s = \tilde{h}_w$, the buttressing must be

$$B^F = 1 + \frac{\left(\frac{\rho_m}{\rho_i}-1\right)\tilde{h}_w\left(2-\tilde{h}_w\right)}{1-\frac{\rho_i}{\rho_w}\lambda^2} \quad \text{for} \quad 0 \leq \tilde{h}_w \leq 1. \tag{63}$$

To have calving, the buttressing must be

$$B^* = \frac{-\frac{\rho_i}{\rho_w}\lambda^2 + \frac{\rho_m}{\rho_i}\tilde{h}_w^2}{1-\frac{\rho_i}{\rho_w}\lambda^2} \quad \text{for} \quad 0 \leq \tilde{h}_w \leq 1. \tag{64}$$

It is clear that the crack depths, B^*, and B^F all converge to the results in the LTG cases when $\lambda = 0$.

2.3.3. Surface crevasse atop a meltwater basal crevasse (DS+MB/MS+MB)

We now extend the previous case to consider a basal crevasse filled with meltwater, e.g. from the subglacial water, underneath a surface crevasse. We follow a similar format to that for the LTG in section 2.2.3. The stress in the ice again has the form of (46), and the crack-depth relation is defined by (51). For the force balance equation, the only change is the water pressure at the ice front in the force balance of (52),

$$\begin{aligned} &\frac{-\left(1-\tilde{d}_s-\tilde{d}_b\right)^2 - 2\frac{\rho_m}{\rho_i}\tilde{h}_w\left(1-\tilde{d}_s-\tilde{d}_b\right) - \frac{\rho_m}{\rho_i}\tilde{h}_w^2 - \frac{\rho_m}{\rho_i}\tilde{d}_b\left(2\tilde{z}_h-\tilde{d}_b\right)}{1-\frac{\rho_i}{\rho_w}\lambda^2} \\ &= -B - \frac{\frac{\rho_i}{\rho_w}\lambda^2}{1-\frac{\rho_i}{\rho_w}\lambda^2}. \end{aligned} \tag{65}$$

Solving (65) with (51) for dimensionless crevasse depths, we find that

$$\begin{aligned} &\text{Surface crack depth:}\quad \tilde{d}_s = 1 + \frac{\rho_m}{\rho_i}\tilde{h}_w - \tilde{z}_h \\ &- \sqrt{\left(1-\frac{\rho_i}{\rho_m}\right)\left[B\left(1-\frac{\rho_i}{\rho_w}\lambda^2\right) + \frac{\rho_i}{\rho_w}\lambda^2 - \frac{\rho_m}{\rho_i}\left(\tilde{z}_h^2 - \left(\frac{\rho_m-\rho_i}{\rho_i}\right)\tilde{h}_w^2\right)\right]} \\ &\text{for}\quad 0 \leq \tilde{h}_w \leq \tilde{z}_h, \end{aligned} \tag{66}$$

$$\begin{aligned} &\text{Basal crack depth:}\quad \tilde{d}_b = \tilde{z}_h - \frac{\rho_i}{\rho_m} \\ &\sqrt{\frac{\rho_m}{\rho_m-\rho_i}\left[B\left(1-\frac{\rho_i}{\rho_w}\lambda^2\right) + \frac{\rho_i}{\rho_w}\lambda^2 - \frac{\rho_m}{\rho_i}\left(\tilde{z}_h^2 - \left(\frac{\rho_m-\rho_i}{\rho_i}\right)\tilde{h}_w^2\right)\right]} \\ &\text{for}\quad 0 \leq \tilde{h}_w \leq \tilde{z}_h. \end{aligned} \tag{67}$$

When the basal crevasse depth is zero, the corresponding buttressing is

$$B^F = \frac{-\frac{\rho_i}{\rho_w}\lambda^2 + \frac{\rho_m}{\rho_i}\left(\frac{\rho_m}{\rho_i}\tilde{z}_h^2 - \frac{\rho_m-\rho_i}{\rho_i}\tilde{h}_w^2\right)}{1-\frac{\rho_i}{\rho_w}\lambda^2} \quad \text{for} \quad 0 \leq \tilde{h}_w \leq \tilde{z}_h. \tag{68}$$

Calving, i.e. $\tilde{D} \equiv \tilde{d}_s + \tilde{d}_b = 1$, occurs when the buttressing number reaches

$$B^* = \frac{-\frac{\rho_i}{\rho_w}\lambda^2 + \frac{\rho_m}{\rho_i}\tilde{z}_h^2}{1-\frac{\rho_i}{\rho_w}\lambda^2} \quad \text{for} \quad 0 \leq \tilde{h}_w \leq \tilde{z}_h. \tag{69}$$

The crack depths, B^*, and B^F converge to the results in the LTG cases when $\lambda = 0$. Note the lack of dependence of the calving stress threshold on the amount of meltwater in the surface crevasse, $\tilde{h}_w$. This is the same situation as the LTG; as in section 2.2.3, for $B^* \leq B \leq B^F$ to hold, this dual crevasse case can only exist when $\tilde{z}_h \geqslant \tilde{h}_w$. Thus, a stable meltwater basal crevasse will not form beneath a meltwater-containing surface crevasse unless $\tilde{z}_h \geqslant \tilde{h}_w$. However, if the meltwater basal crevasse closes because $\tilde{h}_w \geqslant \tilde{z}_h$, the calving threshold would be set by the MS case without a basal crevasse defined in the previous section (64).

2.3.4. Surface crevasse atop a saltwater basal crevasse (DS+SB/MS+SB)

In this section, we will study a simplified version of a saltwater-filled basal crevasse beneath a surface crevasse. Saltwater intrusions have been studied theoretically (Wilson and others, 2020; Robel and others, 2022; Gadi and others, 2023; Bradley and Hewitt, 2024; Ehrenfeucht and others, 2024) and observationally (e.g. Kim and

https://doi.org/10.1017/jog.2025.10068 Published online by Cambridge University Press

others, 2024; Rignot and others, 2024). As the precise form of water pressure and density will not have a simple analytical form and likely evolve with entrainment, tides and grounding line migration, we develop an end-member model for fully saltwater-filled basal crevasses.

Similar to the case of a meltwater-containing surface crevasse on an ice shelf, which combines (25) and (26), we have the crack-depth relation

$$\tilde{d}_s = 1 + \frac{\rho_m}{\rho_i}\tilde{h}_w + \frac{\rho_w - \rho_i}{\rho_i}\tilde{d}_b - \lambda \quad \text{for} \quad 0 \le \tilde{h}_w \le -\frac{\rho_w}{\rho_m}\frac{b}{H}. \tag{70}$$

The dimensionless force-balance equation is

$$\left[-\frac{\rho_m}{\rho_i}\tilde{h}_w^2 - \left(1 - \tilde{d}_s - \tilde{d}_b\right)^2 - 2\frac{\rho_m}{\rho_i}\tilde{h}_w\left(1 - \tilde{d}_s - \tilde{d}_b\right) + \tilde{d}_b\frac{\rho_w}{\rho_i}\left(2\frac{b}{H} + \tilde{d}_b\right)\right] \Big/ \left[1 - \frac{\rho_i}{\rho_w}\lambda^2\right] = -B - \frac{\frac{\rho_i}{\rho_w}\lambda^2}{1 - \frac{\rho_i}{\rho_w}\lambda^2}. \tag{71}$$

Combined, we find that

$$\text{Surface crack depth:} \quad \tilde{d}_s = 1 + \frac{b}{H} + \frac{\rho_m}{\rho_i}\tilde{h}_w - \sqrt{\left(1 - \frac{\rho_i}{\rho_w}\right)\left[B\left(1 - \frac{\rho_i}{\rho_w}\lambda^2\right) + \frac{\rho_m}{\rho_i}\frac{\rho_m - \rho_i}{\rho_i}\tilde{h}_w^2\right]} \quad \text{for} \quad 0 \le \tilde{h}_w \le -\frac{\rho_w}{\rho_m}\frac{b}{H}, \tag{72}$$

$$\text{Basal crack depth:} \quad \tilde{d}_b = -\frac{b}{H} - \frac{\rho_i}{\rho_w}\sqrt{\frac{1}{1 - \frac{\rho_i}{\rho_w}}\left[B\left(1 - \frac{\rho_i}{\rho_w}\lambda^2\right) + \frac{\rho_m}{\rho_i}\frac{\rho_m - \rho_i}{\rho_i}\tilde{h}_w^2\right]} \quad \text{for} \quad 0 \le \tilde{h}_w \le -\frac{\rho_w}{\rho_m}\frac{b}{H}. \tag{73}$$

The dual crack-depth solutions as a function of buttressing are presented in Fig. 8 without surface meltwater $\tilde{h}_w = 0$. The range of buttressing that permits dual crack formation is $B^* \le B \le B^F$, where $B = B^F$ when $\tilde{d}_b = 0$ (denoted by the blue stars in Fig. 8),

$$B^F = \frac{\left(1 - \frac{\rho_i}{\rho_w}\right)\lambda^2 - \frac{\rho_m}{\rho_i}\frac{\rho_m - \rho_i}{\rho_i}\tilde{h}_w^2}{1 - \frac{\rho_i}{\rho_w}\lambda^2} \quad \text{for} \quad 0 \le \tilde{h}_w \le -\frac{\rho_w}{\rho_m}\frac{b}{H}, \tag{74}$$

while if $B = B^*$ then calving occurs ($\tilde{D} \equiv \tilde{d}_s + \tilde{d}_b = 1$; denoted by the yellow stars in Fig. 8),

$$B^* = \frac{\frac{\rho_m}{\rho_i}\left(1 - \frac{\rho_m}{\rho_w}\right)\tilde{h}_w^2}{1 - \frac{\rho_i}{\rho_w}\lambda^2} \quad \text{for} \quad 0 \le \tilde{h}_w \le -\frac{\rho_w}{\rho_m}\frac{b}{H}. \tag{75}$$

There are several interesting limits for this calving threshold. First, if there is no water in the surface crevasse or if $\rho_w = \rho_m$, then the calving threshold is $B^* = 0$ regardless of the value of λ (denoted by the yellow stars in Fig. 8). Thus, if there is no net source of buttressing, the glacier would calve. Second, more meltwater in the surface crack will increase the magnitude of B^*, making ice more vulnerable to calving. Lastly, in the case of $\rho_w = \rho_m$ where the density of the water in the surface and basal crevasse is the same, the calving threshold does not depend on the amount of water in the surface crevasse, h_w. Similar to the meltwater basal crevasse case, this holds as long as this dual crack configuration can stably exist, or $B^* \le B \le B^F$. By evaluating $B^* \le B^F$ with (74) and (75), the stable dual crevasse configuration can exist so long as $\tilde{h}_w \le -\frac{\rho_w}{\rho_m}\frac{b}{H}$. However, if the saltwater basal crevasse closes because $\tilde{h}_w \geqslant -\frac{\rho_w}{\rho_m}\frac{b}{H}$, the calving threshold would be set by the MS case without a basal crevasse defined in the previous section 2.3.2.

2.4. Buttressing and the causes of calving

Much of the results of crevasse depths and calving criteria depend on the buttressing number B (10). In Fig. 4, we used an idealized buttressing distribution $B\left(\frac{x}{L}\right) = 1 - \frac{x}{L}$ to illustrate how buttressing affects crack depths. To understand how buttressing can evolve with time for an MTG on a flat bed and constant thickness, as in (9) the buttressing number (Appendix D) may be written as

$$B(x,t) = \phi\left(\frac{H_M(t)}{H}\right)^2 \frac{1 - \frac{\rho_i}{\rho_w}}{1 - \frac{\rho_i}{\rho_w}\lambda^2} + \frac{\int_x^{x_t}\tau_{bx}(x',t)\,dx' + \int_x^{x_t}\tau_w(x',t)\,dx'}{\frac{1}{2}\left(1 - \frac{\rho_i}{\rho_w}\lambda^2\right)\rho_i g H^2}. \tag{76}$$

The first term is the positive buttressing provided by the floating ice mélange (Amundson and others, 2025; Meng and others, 2025) with porosity ϕ and thickness $H_M(t)$. When mélange thickness is very small, as most times in the summer, the mélange buttressing is negligible. The second term comes from the lateral and basal drag forces exerted on ice, consisting of the force per unit width (into the page) $\int_x^{x_t}\tau_{bx}dx'$ due to the basal drag along the bedrock and the horizontal force per unit width due to the depth-averaged lateral drag on both lateral walls $\int_x^{x_t}\tau_w dx'$. For real glaciers, buttressing may depend on spatially varying drag in 3-dimensions with $\tau_{bx}(x,y)$ and $\tau_w(x,z)$, and bed topography $\rho_i g H \partial_x b$. These buttressing extensions are discussed in Appendix D assuming negligible variation in glacier width along x.

Importantly, different dominant balances between the terms in (76) can lead to a diverse set of calving styles. Seasonal calving behavior observed for Greenland can occur if any of the components altering buttressing (mélange, drag forces, or other potential contributors) vary seasonally. Thus, quantifying the relative magnitude of each term in (76) can help in understanding the calving styles of glaciers.

3. Discussion

In this section, we summarize and interpret our results derived in previous sections, for an ice shelf (Table 2), MTG (Tables 3 and 4) and LTG (setting $\lambda = 0$ in Table 3 and the MS+MB column of Table 4).

Generally, the calving criteria depend on a set of two key dimensionless numbers $\{B, \lambda\}$ and the densities of ice and saltwater. If meltwater is present in either the surface or basal cracks, the calving criteria can depend on two more parameters $\tilde{h}_w, \tilde{z}_h$ and the density of meltwater. The calving regime diagram, Fig. 9a, showcases

https://doi.org/10.1017/jog.2025.10068 Published online by Cambridge University Press

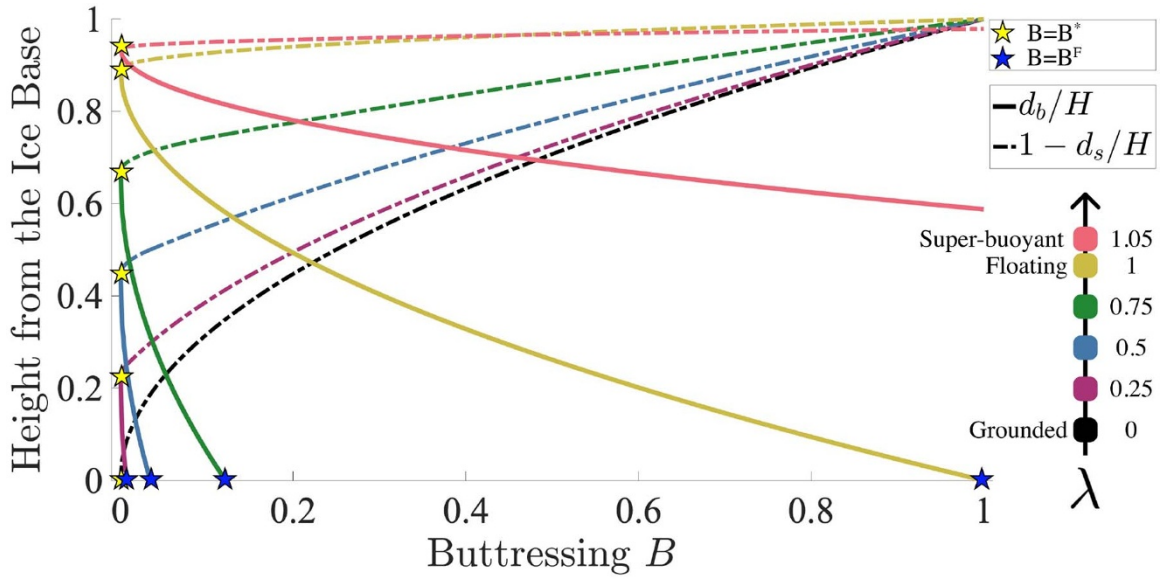

Figure 8. Crevasse-depth solutions for Marine-Terminating Glaciers (MTGs) (58), (72) and (73) as a function of dimensionless buttressing B for dry surface and saltwater basal crevasses (DS+SB). Colors correspond to the dimensionless water level, $\lambda \equiv -\frac{\rho_w}{\rho_i}\frac{b}{H}$. Solid lines are basal crack depths d_b/H measured from the ice base at 0. Dash-dotted lines are surface crack depths d_s/H measured downward from the surface. For all cases with dry surface and saltwater basal crevasses (DS+SB), the calving criterion ($d_s + d_b = H$) of MTGs is $B^* = 0$ (marked with yellow stars) as seen in (75). The unlikely super-buoyant scenario, $\lambda > 1$ (Benn and others, 2017) is represented here with the red curves. Intruding saltwater under grounded MTGs do not form basal crevasses unless $B \leq B^F$, defined by (74) and shown by the blue stars.

Table 2. Crack depths $(\tilde{d}_s, \tilde{d}_b)$, calving criteria B^*, buttressing required for dual crack formation B^F and the corresponding range of $\tilde{h}_w$ for an ice shelf, derived in section 2.1 and illustrated in Figure 3 middle panels. The MS+SB column converges to DS+SB when $\tilde{h}_w = 0$

Case	Dry Surface + Saltwater Basal (DS+SB)	Meltwater Surface + Saltwater Basal (MS+SB)	Meltwater Surface (MS)
$\tilde{d}_s$	$\left(1-\frac{\rho_i}{\rho_w}\right)\left(1-\sqrt{B}\right)$	$\frac{\rho_m}{\rho_i}\tilde{h}_w + \left(1-\frac{\rho_i}{\rho_w}\right)\left(1-\sqrt{B+\frac{\rho_m-\rho_i}{\rho_w-\rho_i}\frac{\rho_m\rho_w}{\rho_i^2}\tilde{h}_w^2}\right)$	$1+\frac{\rho_m}{\rho_i}\tilde{h}_w - \sqrt{B\left(1-\frac{\rho_i}{\rho_w}\right)+\frac{\rho_i}{\rho_w}+\frac{\rho_m}{\rho_i}\left(\frac{\rho_m}{\rho_i}-1\right)\tilde{h}_w^2}$
$\tilde{d}_b$	$\frac{\rho_i}{\rho_w}\left(1-\sqrt{B}\right)$	$\frac{\rho_i}{\rho_w}\left(1-\sqrt{B+\frac{\rho_m-\rho_i}{\rho_w-\rho_i}\frac{\rho_m\rho_w}{\rho_i^2}\tilde{h}_w^2}\right)$	N/A
B^* (Calving criteria)	0	$\frac{\rho_w-\rho_m}{\rho_w-\rho_i}\frac{\rho_m}{\rho_i}\tilde{h}_w^2$	$\left[-\frac{\rho_i}{\rho_w}+\frac{\rho_m}{\rho_i}\tilde{h}_w^2\right] / \left[1-\frac{\rho_i}{\rho_w}\right]$
B^F	1	$1-\frac{\rho_m-\rho_i}{\rho_w-\rho_i}\frac{\rho_m\rho_w}{\rho_i^2}\tilde{h}_w^2$	N/A
$\tilde{h}_w$ range	0	$\left[0, \frac{\rho_i}{\rho_m}\right]$	$\left[\frac{\rho_i}{\rho_m}, 1\right]$

Table 3. Crack depths $(\tilde{d}_s, \tilde{d}_b)$, calving criteria B^*, buttressing required for surface crack formation B^F and the corresponding range of $\tilde{h}_w$ for a surface crevasse on a marine-terminating glacier (MTG), derived in sections 2.3.1 and 2.3.2 and illustrated in Figure 3 left panels. The results converge to an LTG when $\lambda = 0$. The MS column converges to DS when $\tilde{h}_w = 0$.

Case	Dry Surface Crevasse (DS)	Meltwater Surface Crevasse (MS)
$\tilde{d}_s$	$1-\sqrt{B\left(1-\frac{\rho_i}{\rho_w}\lambda^2\right)+\frac{\rho_i}{\rho_w}\lambda^2}$	$1+\frac{\rho_m}{\rho_i}\tilde{h}_w - \sqrt{B\left(1-\frac{\rho_i}{\rho_w}\lambda^2\right)+\frac{\rho_i}{\rho_w}\lambda^2+\frac{\rho_m}{\rho_i}\left(\frac{\rho_m}{\rho_i}-1\right)\tilde{h}_w^2}$
$\tilde{d}_b$	N/A	N/A
B^* (Calving criteria)	$\left[-\frac{\rho_i}{\rho_w}\lambda^2\right] / \left[1-\frac{\rho_i}{\rho_w}\lambda^2\right]$	$\left[-\frac{\rho_i}{\rho_w}\lambda^2+\frac{\rho_m}{\rho_i}\tilde{h}_w^2\right] / \left[1-\frac{\rho_i}{\rho_w}\lambda^2\right]$
B^F	1	$1+\left[\left(\frac{\rho_m}{\rho_i}-1\right)\tilde{h}_w\left(2-\tilde{h}_w\right)\right] / \left[1-\frac{\rho_i}{\rho_w}\lambda^2\right]$
$\tilde{h}_w$ range	0	$[0, 1]$

MTGs, LTGs ($\lambda = 0$) and ISs ($\lambda = 1$), such that the calving criteria can be plotted as a function of B and the dimensionless water level λ. In all cases explored, decreasing the buttressing B eventually leads to calving (dashed curves in Fig. 9a, also illustrated by the cartoons i through iv in b). The effect of the dimensionless water level λ is not as simple, as seen in the bounds for buttressing B^* and B^F in Tables 2–4 and shown by the dashed and solid curves in Fig. 9a, respectively.

3.1. Dry surface crevasse atop a saltwater basal crevasse (DS+SB)

In the case of a dry surface crevasse atop a saltwater basal crevasse (DS+SB) with constant ice thickness and a flat bed, the calving criterion is $B^* = 0$ regardless of the dimensionless water level λ (dashed purple line in Fig. 9a and cartoon b-iii). Since the saltwater basal crevasse has its pressure driven by the proglacial water

https://doi.org/10.1017/jog.2025.10068 Published online by Cambridge University Press

Table 4. Crack depths $(\tilde{d}_s, \tilde{d}_b)$, calving criteria B^*, buttressing required for dual crack formation B^F and the corresponding range of $\tilde{h}_w$ for dual cracks on a marine-terminating glacier (MTG), derived in sections 2.3.3 and 2.3.4 and illustrated in Figure 3 middle and right panels. The results converge to DS+MB/SB when $\tilde{h}_w = 0$. The MS+MB column converges to an LTG when $\lambda = 0$. The MS+SB column converges to an IS when ice is at flotation $\lambda = 1$, $b/H = -\rho_i/\rho_w$.

Case	Meltwater Surface + Meltwater Basal (MS+MB)	Meltwater Surface + Saltwater Basal (MS+SB)
$\tilde{d}_s$	$1 + \frac{\rho_m}{\rho_i}\tilde{h}_w - \tilde{z}_h - \sqrt{\left(1-\frac{\rho_i}{\rho_m}\right)\left[B\left(1-\frac{\rho_i}{\rho_w}\lambda^2\right) + \frac{\rho_i}{\rho_w}\lambda^2 - \frac{\rho_m}{\rho_i}\left(\tilde{z}_h^2 - \left(\frac{\rho_m-\rho_i}{\rho_i}\right)\tilde{h}_w^2\right)\right]}$	$1 + \frac{b}{H} + \frac{\rho_m}{\rho_i}\tilde{h}_w - \sqrt{\left(1-\frac{\rho_i}{\rho_w}\right)\left[B\left(1-\frac{\rho_i}{\rho_w}\lambda^2\right) + \frac{\rho_m}{\rho_i}\frac{\rho_m-\rho_i}{\rho_i}\tilde{h}_w^2\right]}$
$\tilde{d}_b$	$\tilde{z}_h - \frac{\rho_i}{\rho_m}\sqrt{\frac{\rho_m}{\rho_m-\rho_i}\left[B\left(1-\frac{\rho_i}{\rho_w}\lambda^2\right) + \frac{\rho_i}{\rho_w}\lambda^2 - \frac{\rho_m}{\rho_i}\left(\tilde{z}_h^2 - \left(\frac{\rho_m-\rho_i}{\rho_i}\right)\tilde{h}_w^2\right)\right]}$	$-\frac{b}{H} - \frac{\rho_i}{\rho_w}\sqrt{\frac{1}{1-\frac{\rho_i}{\rho_w}}\left[B\left(1-\frac{\rho_i}{\rho_w}\lambda^2\right) + \frac{\rho_m}{\rho_i}\frac{\rho_m-\rho_i}{\rho_i}\tilde{h}_w^2\right]}$
B^* (Calving criteria)	$\left[-\frac{\rho_i}{\rho_w}\lambda^2 + \frac{\rho_m}{\rho_i}\tilde{z}_h^2\right] / \left[1-\frac{\rho_i}{\rho_w}\lambda^2\right]$	$\left[\frac{\rho_m}{\rho_i}\left(1-\frac{\rho_m}{\rho_w}\right)\tilde{h}_w^2\right] / \left[1-\frac{\rho_i}{\rho_w}\lambda^2\right]$
B^F	$\left[-\frac{\rho_i}{\rho_w}\lambda^2 + \frac{\rho_m}{\rho_i}\left(\frac{\rho_m}{\rho_i}\tilde{z}_h^2 - \frac{\rho_m-\rho_i}{\rho_i}\tilde{h}_w^2\right)\right] / \left[1-\frac{\rho_i}{\rho_w}\lambda^2\right]$	$\left[\left(1-\frac{\rho_i}{\rho_w}\right)\lambda^2 - \frac{\rho_m}{\rho_i}\frac{\rho_m-\rho_i}{\rho_i}\tilde{h}_w^2\right] / \left[1-\frac{\rho_i}{\rho_w}\lambda^2\right]$
$\tilde{h}_w$ range	$[0, \tilde{z}_h]$	$\left[0, -\frac{\rho_w}{\rho_m}\frac{b}{H}\right]$

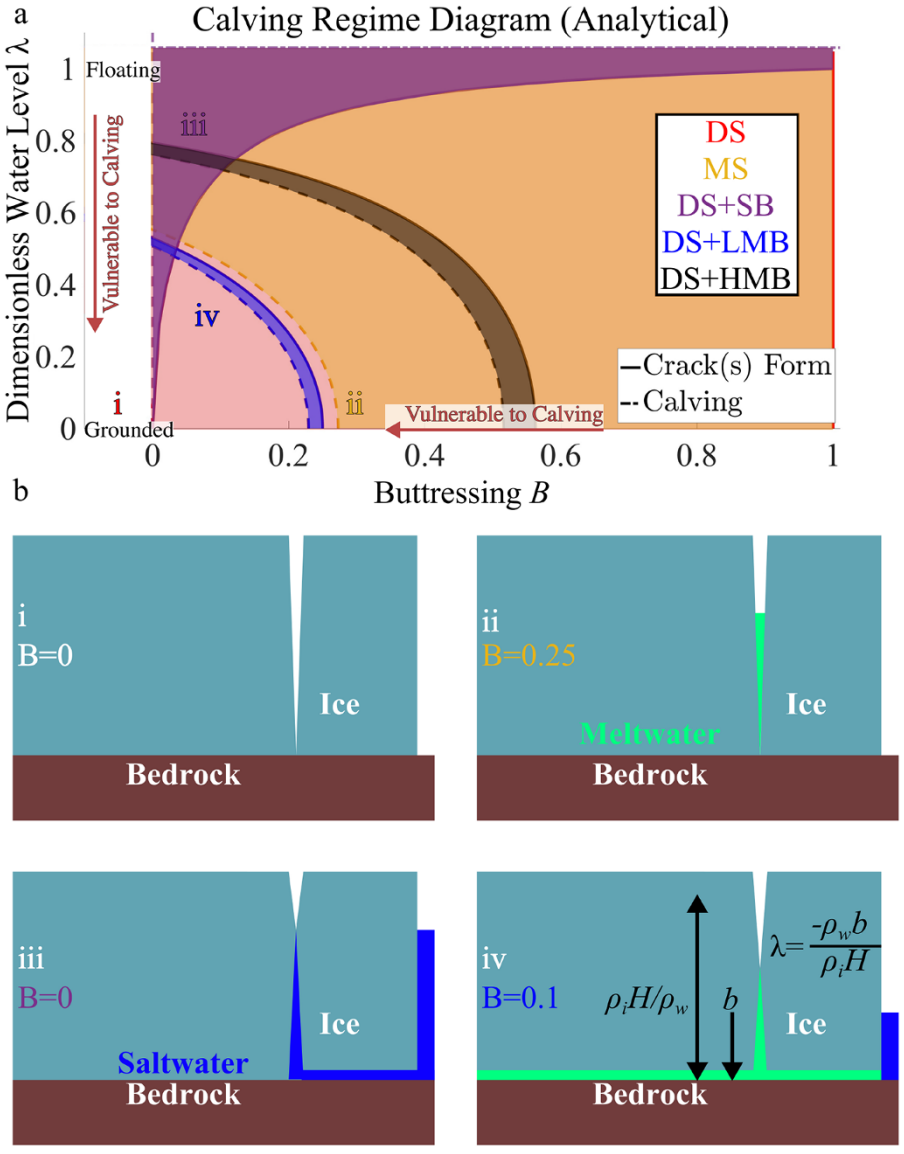

Figure 9. Panel a displays the calving regime diagram as a function of the dimensionless buttressing B and the dimensionless water level $\lambda \equiv -\rho_w b/(\rho_i H)$ ($=0$ for a land-terminating glacier with a flat bed; $=1$ for an ice shelf). The onset of calving and crack initiation is shown by the dashed curves and bold curves, respectively, with plausible crack(s) existence living within the shaded regions. We use head height values of $\tilde{z}_h = \rho_i/(2\rho_m)$ for DS+LMB in blue and $\tilde{z}_h = 3\rho_i/(4\rho_m)$ for DS+HMB in black. Panel b shows four cases of glaciers reaching the calving threshold corresponding to different locations in panel a, labeled as i to iv, with ocean saltwater shown in blue and freshwater shown in green. DS = Dry Surface, MS = Meltwater Surface, DS+SB = Dry Surface and Saltwater Basal, DS+L(H)MB = Dry Surface and Low (High)-pressure Meltwater Basal.

height, lowering the dimensionless water level λ will also decrease the pressure in the basal crevasse. Hence, decreasing the water level will decrease the basal crack depth, as crossing the solid purple line in Fig. 9a represents transitioning from dual crevasses to a dry surface crevasse without a basal crevasse (DS).

3.2. *Dry surface crevasse atop a meltwater basal crevasse (DS+MB)*

For a basal crevasse filled with subglacial meltwater, the water pressure in the basal crevasse can be set by the subglacial hydrology,

https://doi.org/10.1017/jog.2025.10068 Published online by Cambridge University Press

and thus is decoupled from the water level λ. But lowering the water level λ will promote meltwater basal crevasse-driven calving. For example, Figs. 9a and A1 in Appendix A show the buttressing bounds for a dry surface crevasse atop a meltwater basal crevasse (DS+MB) in blue and black: decreasing the dimensionless water level λ while keeping buttressing B fixed can result in basal crevasse formation and calving. Thus, increasing the water level toward flotation ($\lambda = 1$) will increase the supporting force from the ocean acting on the ice front and stabilize the glacier.

The set of two curves, blue and black, in Fig. 9a shows the sensitivity of meltwater basal crevasses to the piezometric head height $\tilde{z}_h$. The head height in the basal crevasse analyzed in this paper depends on the subglacial hydrology, which varies spatiotemporally (e.g. Figure S1 of Harper and others (2010)) and is beyond the scope of this paper. The lower-pressure (LMB) blue curves in Fig. 9a correspond to $\tilde{z}_h = \frac{1}{2}\frac{\rho_i}{\rho_m}$, while the higher-pressure (HMB) black curves assume an arbitrarily high pressure $\tilde{z}_h = \frac{3}{4}\frac{\rho_i}{\rho_m}$, which substantially reduces the critical stresses (increase the critical buttresssing) required for calving (black dashed curve in Fig. 9a), weakening the glacier. Thus, the sensitivity of calving to subglacial water pressure is strong. Additionally, the basal crevasse formation threshold B^F strongly depends on the head height $\tilde{z}_h$. Basal crevasses on LTGs have been observed in Ensminger and others (2001), Fountain and others (2005), Harper and others (2010) and surge-type glaciers (Rea and Evans, 2011).

3.3. Dry (DS) or meltwater-containing surface crevasse (MS) without a basal crevasse

Finally, we consider surface crevasses, dry (DS) and with meltwater (MS), without basal crevasses. The simplest case is the LTG ($\lambda = 0$), shown by Fig. 9b-i and b-ii: a dry surface crevasse (DS) will calve at $B = 0$, as shown by i, while a meltwater-containing surface crevasse (MS) with $\tilde{h}_w = \frac{1}{2}$ will calve at $B^* = \frac{\rho_m}{\rho_i}\tilde{h}_w^2$, as shown by (ii). Note that the HFB model predicts glaciers to be much more vulnerable to calving compared with the Zero-Stress approximation. The Zero-Stress approximation predicts calving at $B^* = -1$ and $B^* = 2\frac{\rho_m}{\rho_i}\tilde{h}_w - 1$ for the same dry and meltwater cases described above. In terms of critical calving stresses for dry surface crevasses on a constant thickness LTG, the amount of tensile resistive stress $\overline{R}_{xx}$ required for calving for the HFB model is only half that of the Zero-Stress approximation, similar to previous findings for floating ISs (Buck, 2023, Coffey and others, 2024).

For meltwater hydrofracture-induced calving, we analyze if more tension (less buttressing) is required for calving for the same amount of meltwater $\tilde{h}_w$ in HFB than the Zero-Stress approximation. The two calving criteria, $B^* = \frac{\rho_m}{\rho_i}\tilde{h}_w^2$ for HFB and $B^* = 2\frac{\rho_m}{\rho_i}\tilde{h}_w - 1$ for Zero-Stress, predict the same calving stress threshold at $\tilde{h}_w = 1 - \sqrt{1 - \frac{\rho_i}{\rho_m}} \approx 0.72$. For calving to occur with the meltwater in a surface crevasse less than 72% of the ice thickness, less tensile stress (more buttressing) can lead to calving in HFB than the Zero-Stress approximation.

3.4. Model limitations

Our HFB calving models have a list of assumptions, which are all also used by the original Zero-Stress approximation (Nye, 1955), including the (1) zero material strength (Appendix C.1), (2) no elastic deformation associated with lake-induced flexure and tidal or wave perturbations (Appendix C.2), (3) constant density (Appendix C.3), (4) neglected thermomechanical effects (Appendix C.4) and (5) neglected ice rheological effects (Appendix C.5). Additionally, as mentioned in Appendix D, the analysis for MTGs in this paper requires the idealistic assumptions of constant thickness and flat bed slope. The consideration of these aforementioned effects is beyond the scope of the current study. Note that assumptions (2)-(5) are also commonly assumed by existing fracture models like LEFM (van der Veen, 1998a, 1998b; Jiménez and Duddu, 2018; Lai and others, 2020), the Zero-Stress approximation (Nye, 1955; Jezek, 1984; Benn and others, 2007a; Nick and others, 2010), and HFB for constant-thickness ISs (Buck, 2023; Coffey and others, 2024). While important for crack depths, temperature dependence has been found to be negligible for the stress criteria for calving when $\tilde{D} = 1$ in Coffey and others (2024), and is not considered in this paper.

3.5. Comparison with existing ideas

3.5.1. Diverse calving styles

The wide-ranging calving styles can be conceptually attributed to the fact that different terms in the HFB equation dominate in varying scenarios. The method of dominant balances is the idea that the equations may be described by the balance of the two (or more) most important terms. For example, the dominant balances of different terms in the Navier-Stokes equation can describe wide-ranging phenomena from glacial flow to hurricanes. Similarly, different combinations of the dominant terms in the HFB (3) across various glacial settings can exhibit a wide range of calving styles via different dominant balances between the horizontal hydrostatic forces acting on the crevasse wall and calving front, and various buttressing forces (9) such as the basal drag, lateral drag and mélange buttressing. This can qualitatively explain a diverse range of calving styles, as listed in the following.

HFB can capture the seasonal signature of calving through the dependence on a seasonal buttressing force. For Greenland MTG that experience a loss of buttressing in summer, through thinner mélange (Xie and others, 2019; Meng and others, 2025) and reduced drag, calving occurs more frequently in the summer and thus exhibits seasonality (Zhang and others, 2023; Greene and others, 2024). Similarly, if a grounded glacier experiences saltwater intrusions or begins to float, the basal drag may be substantially reduced and push the system toward calving. While not modeled fully in this paper, large geometric effects at the ice front, such as a buoyant foot, water line melt, or undercutting, may lead to a mixed-mode, flexurally-driven or shear-driven calving style (Wagner and others, 2014; 2016; Slater and others, 2017; How and others, 2019; Sartore and others, 2025).

On ISs, if the basal drag and mélange or sea ice buttressing are negligible, calving occurs when the lateral drag, the major source of buttressing, is lost as ice passes by and loses contact with land, such as an ice rise. This can trigger rifting near the ice rise location, causing tabular icebergs, as seen around the Roosevelt Island on the Ross Ice Shelf and the Gipps Ice Rise on the Larsen C Ice Shelf. A similar effect has been modeled at Sermeq Kujalleq (Store Glacier), Greenland (Benn and others, 2023). However, we note that our HFB crevasse-depth model in its current form is more appropriate to describe rift initiation from vertical crevasses (Coffey and others, 2024), as it does not describe horizontal rift propagation (Lipovsky, 2020) and its timescales (Bassis and others, 2007). Lastly, grounding zone saltwater intrusions by tides (Rignot and others, 2024), causing reduced basal drag and varying water

https://doi.org/10.1017/jog.2025.10068 Published online by Cambridge University Press

density (Wilson and others, 2020; Robel and others, 2022; Bradley and Hewitt, 2024), may impact the crevasse formation and calving threshold.

While each of these examples has been previously studied, the key point is that the force-balance equation can serve as a unified fundamental equation to describe a range of diverse calving styles.

3.5.2. Dependence on thickness H

One important feature of HFB, the Zero-Stress approximation, and LEFM is that the calving thresholds scale linearly with the ice thickness H (Coffey and others, 2024). Physically speaking, a greater ice thickness results in higher lithostatic stresses, meaning the ice needs correspondingly larger tensile stresses to calve. However, this is not the case when a constant critical stress threshold for different ice thicknesses is assumed for calving. When calving is set to occur above a critical stress or thickness, we would expect runaway behavior because the ice is generally thicker upstream and the depth-averaged deviatoric stress scales with H (Haseloff and Sergienko, 2022) (e.g. Marine Ice Cliff Instability (MICI) (Bassis and Walker, 2012; DeConto and Pollard, 2016)). Future theoretical work implementing HFB with MICI is important for understanding ice cliff stability.

3.5.3. Comparison with existing calving laws

HFB, Zero-Stress and LEFM can all be considered as "crevasse-depth" calving laws (Benn and others, 2007b; 2023; Choi and others, 2018; Wilner and others, 2023) in that calving occurs when the crevasse (surface plus basal) depth equals the ice thickness. Most calving laws involve tuning unmeasurable parameters, e.g. the parameter σ_{max} in the von Mises law (Morlighem and others, 2016; Choi and others, 2018; Downs and others, 2023; Wilner and others, 2023). Our results involve measurable and known parameters (stresses and water level), except for the meltwater-filled crevasse cases. Our analytical HFB model shows that the fundamental parameters that govern calving are the in-situ buttressing stresses B, the dimensionless water level λ and the densities of ice and water in the crevasses. If meltwater is present in the crevasses, both the surface meltwater depth $\tilde{h}_w$ and the meltwater head height $\tilde{z}_h$ will affect the calving criteria. Thus, our HFB formulation can yield diverse calving criteria, suggesting that using one universal threshold value of stress for all glacier calving is not appropriate. Multiple thresholds must be used to effectively capture the various scenarios, including but not limited to those mentioned in this paper. Further work comparing these criteria with observations and integration in numerical models with additional effects (Bassis and Ma, 2015; Berg and Bassis, 2022) will be informative. An initial comparison between the HFB theory and the observed ice-shelf rift locations is available in Coffey and others (2024).

Recent work (Zarrinderakht and others, 2022; Coffey and others, 2024) shows that LEFM for a surface or basal crevasse gives stress thresholds for ice shelf calving that can be understood through torque balance, $\Sigma\tau = 0$. It has also been shown and argued (Yu and others, 2017; Jiménez and Duddu, 2018; Huth and others, 2021; Zarrinderakht and others, 2022; Coffey and others, 2024) that the hydrostatic ocean restoring force can not be neglected. In Appendix B, we show that the calving stress from the conventional LEFM solution used for isolated ice shelf basal crevasses (van der Veen, 1998a) written with torque balance (Zarrinderakht and others, 2022) can be modified to consider the ocean restoring force and allow for ice shelf deflection, thus predicting the same calving stress threshold as HFB.

4. Conclusion

In this paper, we generalize the HFB fracture model (Buck, 2023; Coffey and others, 2024) across ISs, LTGs and MTGs. We examine six tensile crack configurations in HFB defined in Fig. 3, which lead to different calving stress thresholds (see Tables 2, 3 and 4). Our generalized HFB model yields analytical solutions for crack depths and the calving criteria. We show that in the absence of meltwater in the surface or basal cracks, the calving criteria fundamentally depend on the dimensionless buttressing force B, the dimensionless water level $\lambda \equiv \frac{-\rho_w b}{\rho_i H}$, as well as the ice to saltwater density ratio (constant). These parameters can either be measured or calculated. In the cases when meltwater is present in crevasses, a few more parameters play a role: dimensionless meltwater depth $\tilde{h}_w \equiv h_w/H$ in the surface crevasse, dimensionless head height $\tilde{z}_h \equiv z_h/H$ in the meltwater basal crevasse, and the ice to meltwater density ratio (constant). In other words, with a specified $\{B, \lambda, \tilde{h}_w, \tilde{z}_h\}$ and crack configuration, an HFB calving criteria can be obtained analytically. Our result is summarized in Tables 2, 3 and 4.

The generalized crevasse-depth calving laws using HFB have great explanatory power. In general, lower buttressing B can lead to calving in every crack configuration explored. Similarly, lowering the dimensionless water level λ has the same effect, except in the case of calving driven by saltwater basal crevasses. For LTGs with dry surface crevasses (DS), and MTGs and ISs with dry surface crevasses and saltwater-filled basal crevasses (DS+SB), the calving criterion is simply no buttressing, $B^* = 0$, regardless of the dimensionless water level λ. Thus, this result of MTGs converges to ISs and LTGs with a flat bed when $\lambda = 1$ and 0, respectively.

Our result indicates that there is generally no reason to expect a universal threshold value of calving stress for all glaciers due to each crack configuration's (Fig. 3) varying dependence on the parameters $B, \lambda, \tilde{h}_w, \tilde{z}_h$. HFB can be used to model a range of calving styles in a unified framework. For example, the seasonality of calving in Greenland can be caused by a decrease of buttressing in the summer via $B = B^* = 0$. This loss of summer buttressing can be attributed to various sources, e.g. reduced basal and lateral drag, thinner mélange and their combinations. We note that the HFB calving threshold only depends on the net buttressing B and is agnostic to the buttressing loss mechanisms. Climate warming is a threat as the calving criteria is very sensitive to the surface meltwater depth $\tilde{h}_w$ and subglacial meltwater head height $\tilde{z}_h$.

Modeling of the diverse calving styles (Alley and others, 2023; Bassis and others, 2024) is a challenge. Our HFB model can analytically predict transitions between six crack configurations across ISs, MTGs and LTGs. The dynamical coupling between HFB and an ice flow model to assess calving behavior during glacial retreat is a topic for future study.

Acknowledgements. Ching-Yao Lai acknowledges partial funding from NSF's Office of Polar Programs through OPP-2344690.

Competing interests. The authors declare that they have no conflict of interest.

References

Alley R and 8 others (2023) Iceberg calving: Regimes and transitions. *Annual Review of Earth and Planetary Sciences* **51**(1), 189–215. doi: 10.1146/annurev-earth-032320-110916

Amundson JM, Fahnestock M, Truffer M, Brown J, Lüthi MP and Motyka RJ (2010) Ice mélange dynamics and implications for terminus stability,

Jakobshavn Isbræ, Greenland. *Journal of Geophysical Research: Earth Surface* **115**(F1), F01005. doi: 10.1029/2009JF001405

Amundson JM, Robel AA, Burton JC and Nissanka K (2025) A quasi-one-dimensional ice mélange flow model based on continuum descriptions of granular materials. *The Cryosphere* **19**(1), 19–35. doi: 10.5194/tc-19-19-2025

Anderson TL (2017) fourth edition *Fracture Mechanics: Fundamentals and Applications, Fourth Edition.*, Boca Raton: CRC Press

Banwell AF, MacAyeal DR and Sergienko OV (2013) Breakup of the Larsen B ice shelf triggered by chain reaction drainage of supraglacial lakes. *Geophysical Research Letters* **40**(22), 5872–5876. doi: 10.1002/2013GL057694

Banwell AF, Willis IC, Stevens LA, Dell RL and MacAyeal DR (2024) Observed meltwater-induced flexure and fracture at a doline on george vi ice shelf, antarctica. *Journal of Glaciology* **70**, e47. doi: 10.1017/jog.2024.31

Bassis J and Ma Y (2015) Evolution of basal crevasses links ice shelf stability to ocean forcing. *Earth and Planetary Science Letters* **409**, 203–211. doi: 10.1016/j.jpgl.2014.11.003

Bassis JN, Berg B, Crawford AJ and Benn DI (2021) Transition to marine ice cliff instability controlled by ice thickness gradients and velocity. *Science* **372**(6548), 1342–1344. doi: 10.1126/science.abf6271

Bassis JN and 9 others (2024) Stability of ice shelves and ice cliffs in a changing climate. *Annual Review of Earth and Planetary Science* **52**, 221–247. doi: 10.1146/annurev-earth-040522-122817

Bassis JN and 7 others (2007) Seismicity and deformation associated with ice-shelf rift propagation. *Journal of Glaciology* **53**(183), 523–536. doi: 10.3189/002214307784409207

Bassis JN and Walker CC (2012) Upper and lower limits on the stability of calving glaciers from the yield strength envelope of ice. *Proceedings of the Royal Society A: Mathematical, Physical and Engineering Sciences* **468**(2140), 913–931. doi: 10.1098/rspa.2011.0422

Bažant ZP, Le JL and Salviato M (2021) *Quasibrittle Fracture Mechanics and Size Effect: A First Course.* Oxford: Oxford University Press. doi: 10.1093/oso/9780192846242.001.0001

Benn DI and 7 others (2017) Melt-under-cutting and buoyancy-driven calving from tidewater glaciers: new insights from discrete element and continuum model simulations. *Journal of Glaciology* **63**(240), 691–702. doi: 10.1017/jog.2017.41

Benn DI, NRJ Hulton and RH Mottram (2007a) 'Calving laws', 'sliding laws' and the stability of tidewater glaciers. *Annals of Glaciology*, **46**, 123–130. doi: 10.3189/172756407782871161

Benn DI, Warren CR and Mottram RH (2007b) Calving processes and the dynamics of calving glaciers. *Earth-Science Reviews* **82**(3), 143–179. doi: 10.1016/j.earscirev.2007.02.002

Benn DI and 8 others (2023) Controls on calving at a large Greenland tidewater glacier: stress regime, self-organised criticality and the crevasse-depth calving law. *Journal of Glaciology* **69**(278), 2059–2074. doi: 10.1017/jog.2023.81

Berg B and Bassis J (2022) Crevasse advection increases glacier calving. *Journal of Glaciology* **68**(271), 977–986. doi: 10.1017/jog.2022.10

Bradley AT and Hewitt IJ (2024) Tipping point in ice-sheet grounding-zone melting due to ocean water intrusion. *Nature Geoscience* **17**(7), 631–637. doi: 10.1038/s41561-024-01465-7

Buck WR (2023) The role of fresh water in driving ice shelf crevassing, rifting and calving. *Earth and Planetary Science Letters* **624**, 118444. doi: 10.1016/j.jpgl.2023.118444

Buck WR (2024) The effect of ice shelf rheology on shelf edge bending. *The Cryosphere* **18**(9), 4165–4176. doi: 10.5194/tc-18-4165-2024

Buck WR and Lai CY (2021) Flexural control of basal crevasse opening under ice shelves. *Geophysical Research Letters* **48**(8), e2021GL093110. doi: 10.1029/2021GL093110

Chase DL, Lai CY and Stone HA (2021) Relaxation of a fluid-filled blister on a porous substrate. *Physical Review Fluids* **6**, 084101. doi: 10.1103/PhysRevFluids.6.084101

Choi Y, Morlighem M, Wood M and Bondzio JH (2018) Comparison of four calving laws to model Greenland outlet glaciers. *The Cryosphere* **12**(12), 3735–3746. doi: 10.5194/tc-12-3735-2018

Christie FDW, Benham TJ, Batchelor CL, Rack W, Montelli A and Dowdeswell JA (2022) Antarctic ice-shelf advance driven by anomalous atmospheric and sea-ice circulation. *Nature Geoscience* **15**(5), 356–362. doi: 10.1038/s41561—00938-x

Clayton T, Duddu R, Hageman T and Martínez-Pañeda E (2024) The influence of firn layer material properties on surface crevasse propagation in glaciers and ice shelves. *The Cryosphere* **18**(12), 5573–5593. doi: 10.5194/tc-18-5573-2024

Clerc F, Minchew BM and Behn MD (2019) Marine ice cliff instability mitigated by slow removal of ice shelves. *Geophysical Research Letters* **46**(21), 12108–12116. doi: 10.1029/2019GL084183

Coffey NB, Lai CY, Wang Y, Buck WR, Surawy-Stepney T and Hogg AE (2024) Theoretical stability of ice shelf basal crevasses with a vertical temperature profile. *Journal of Glaciology* **70**, e64. doi: 10.1017/jog.2024.52

Coffey NB and 6 others (2022) Enigmatic surface rolls of the ellesmere ice shelf. *Journal of Glaciology* **68**(271), 867–878. doi: 10.1017/jog.2022.3

Crouch SL (1976) Solution of plane elasticity problems by the displacement discontinuity method. i. infinite body solution. *International Journal for Numerical Methods in Engineering* **10**(2), 301–343. doi: 10.1002/nme.1620100206

Crouch SL and Starfield AM (1983) *Boundary Element Methods in Solid Mechanics: With Applications in Rock Mechanics and Geological Engineering.*, London: Allen & Unwin.

Cuffey KM and Paterson WSB (2010) *The Physics of Glaciers*. Amsterdam: Academic Press.

Dahlen F and Tromp J (1998) *Theoretical Global Seismology.*, Princeton, NJ: Princeton University Press

DeConto RM and Pollard D (2016) Contribution of Antarctica to past and future sea-level rise. *Nature* **531**(7596), 591–597. doi: 10.1038/nature17145

Downs J, Brinkerhoff D and Morlighem M (2023) Inferring time-dependent calving dynamics at Helheim Glacier. *Journal of Glaciology* **69**(274), 381–396. doi: 10.1017/jog.2022.68

Dupont TK and Alley RB (2005) Assessment of the importance of ice-shelf buttressing to ice-sheet flow. *Geophysical Research Letters* **32**(4), L04503. doi: 10.1029/2004GL022024

Ehrenfeucht S, Rignot E and Morlighem M (2024) Seawater intrusion in the observed grounding zone of Petermann Glacier causes extensive retreat. *Geophysical Research Letters* **51**(12), e2023GL107571. doi: 10.1029/2023GL107571

Ensminger SL, Alley RB, Evenson EB, Lawson DE and Larson GJ (2001) Basal-crevasse-fill origin of laminated debris bands at matanuska glacier, alaska, u.s.a. *Journal of Glaciology* **47**(158), 412–422. doi: 10.3189/172756501781832007

Fountain AG, Jacobel RW, Schlichting R and Jansson P (2005) Fractures as the main pathways of water flow in temperate glaciers. *Nature* **433**(7026), 618–621. doi: 10.1038/nature03296

Fox-Kemper B and 17 others (2021) Ocean, Cryosphere and Sea Level Change. Cambridge University Press. *Climate Change 2021: The Physical Science Basis. Contribution of Working Group I to the Sixth Assessment Report of the Intergovernmental Panel on Climate Change*, pp. 1211–1362.

Freed-Brown J, JM Amundson, DR MacAyeal and WW Zhang (2012) Blocking a wave: frequency band gaps in ice shelves with periodic crevasses. *Annals of Glaciology* **53**(60), 85–89. doi: 10.3189/2012AoG60A120

Frost HJ (2001) Mechanisms of crack nucleation in ice. *Engineering Fracture Mechanics* **68**(17), 1823–1837. doi: 10.1016/S0013–(01)00036–4

Gadi R, Rignot E and Menemenlis D (2023) Modeling ice melt rates from seawater intrusions in the grounding zone of Petermann Gletscher, Greenland. *Geophysical Research Letters* **50**(24), e2023GL105869. doi: 10.1029/2023GL105869

Gao Y, Ghosh G, Jiménez S and Duddu R (2023) A finite-element-based cohesive zone model of water-filled surface crevasse propagation in floating ice tongues. *Computing in Science & Engineering* **25**(3), 8–16. doi: 10.1109/MCSE.2023.3315661

Gomez-Fell R, Rack W, Purdie H and Marsh O (2022) Parker Ice Tongue collapse, Antarctica, triggered by loss of stabilizing land-fast sea ice. *Geophysical Research Letters* **49**(1), e2021GL096156. doi: 10.1029/2021GL096156

Greene CA, Gardner AS, Wood M and Cuzzone JK (2024) Ubiquitous acceleration in Greenland Ice Sheet calving from 1985 to 2022. *Nature* **625**(7995), 523–528. doi: 10.1038/s41586-023-06863-2

Gudmundsson GH (2013) Ice-shelf buttressing and the stability of marine ice sheets. *The Cryosphere* **7**(2), 647–655. doi: 10.5194/tc-7-647-2013

Hageman T, Mejía J, Duddu R and Martínez-Pañeda E (2024) Ice viscosity governs hydraulic fracture that causes rapid drainage of supraglacial lakes. *The Cryosphere* **18**(9), 3991–4009. doi: 10.5194/tc-18-3991-2024

Harper JT, Bradford JH, Humphrey NF and Meierbachtol TW (2010) Vertical extension of the subglacial drainage system into basal crevasses. *Nature* **467**(7315), 579–582. doi: 10.1038/nature09398

Haseloff M and Sergienko OV (2022) Effects of calving and submarine melting on steady states and stability of buttressed marine ice sheets. *Journal of Glaciology* **68**(272), 1149–1166. doi: 10.1017/jog.2022.29

Hetényi M and Hetbenyi MI (1946) *Beams on Elastic Foundation: Theory With Applications in the Fields of Civil and Mechanical engineering*, **16**Ann Arbor, MI: University of Michigan Press.

How P and 8 others (2019) Calving controlled by melt-under-cutting: detailed calving styles revealed through time-lapse observations. *Annals of Glaciology* **60**(78), 20–31. doi: 10.1017/aog.2018.28

Huth A, Duddu R and Smith B (2021) A Generalized Interpolation Material Point Method for Shallow Ice Shelves. 2: Anisotropic Nonlocal Damage Mechanics and Rift Propagation. *Journal of Advances in Modeling Earth Systems* **13**(8), e2020MS002292. doi: 10.1029/2020MS002292

Indrigo C, Dow CF, Greenbaum JS and Morlighem M (2021) Drygalski ice tongue stability influenced by rift formation and ice morphology. *Journal of Glaciology* **67**(262), 243–252. doi: 10.1017/jog.2020.99

Jansen D, Luckman A, Kulessa B, Holland PR and King EC (2013) Marine ice formation in a suture zone on the Larsen C ice shelf and its influence on ice shelf dynamics. *Journal of Geophysical Research: Earth Surface* **118**(3), 1628–1640. doi: 10.1002/jgrf.20120

Jezek KC (1984) A modified theory of bottom crevasses used as a means for measuring the buttressing effect of ice shelves on inland ice sheets. *Journal of Geophysical Research: Solid Earth* **89**(B3), 1925–1931. doi: 10.1029/JB089iB03p01925

Jiménez S and Duddu R (2018) On the evaluation of the stress intensity factor in calving models using linear elastic fracture mechanics. *Journal of Glaciology* **64**(247), 759–770. doi: 10.1017/jog.2018.64

Khazendar A, Rignot E and Larour E (2011) Acceleration and spatial rheology of Larsen C ice shelf, antarctic peninsula. *Geophysical Research Letters* **38**(9), L09502. doi: 10.1029/2011GL046775

Kim JH, Rignot E and Holland D (2024) Seawater intrusion at the grounding line of Jakobshavn Isbræ, Greenland, from terrestrial radar interferometry. *Geophysical Research Letters* **51**(6), e2023GL106181. doi: 10.1029/2023GL106181Holland D

Kulessa B, Jansen D, Luckman AJ, King EC and Sammonds PR (2014) Marine ice regulates the future stability of a large Antarctic ice shelf. *Nature Communications* **5**(1), 3707. doi: 10.1038/ncomms4707

Lai CY and 7 others (2020) Vulnerability of antarctica's ice shelves to meltwater-driven fracture. *Nature* **584**, 574–578. doi: 10.1038/s41586-020-2627-8

Lai CY and 6 others (2021) Hydraulic transmissivity inferred from ice-sheet relaxation following Greenland supraglacial lake drainages. *Nature Communications* **12**(1), 3955. doi: 10.1038/s41467-021-24186-6

Lawn B (1993) *Fracture of Brittle Solids*, 2nd Edn. Cambridge Solid State Science Series. Cambridge: Cambridge University Press. doi: 10.1017/CBO9780511623127

Lawrence JD and 15 others (2023) Crevasse refreezing and signatures of retreat observed at Kamb Ice Stream grounding zone. *Nature Geoscience* **16**(3), 238–243. doi: 10.1038/s41561—01129-y

Levermann A, Albrecht T, Winkelmann R, Martin MA, Haseloff M and Joughin I (2012) Kinematic first-order calving law implies potential for abrupt ice-shelf retreat. *The Cryosphere* **6**(2), 273–286. doi: 10.5194/tc-6-273-2012

Lipovsky BP (2020) Ice shelf rift propagation: stability, three-dimensional effects, and the role of marginal weakening. *The Cryosphere* **14**(5), 1673–1683. doi: 10.5194/tc-14-1673-2020

Litwin KL, Zygielbaum BR, Polito PJ, Sklar LS and Collins GC (2012) Influence of temperature, composition, and grain size on the tensile failure of water ice: Implications for erosion on titan. *Journal of Geophysical Research: Planets* **117**(E8), E08013. doi: 10.1029/2012JE004101

Luckman A, Jansen D, Kulessa B, King EC, Sammonds P and Benn DI (2012) Basal crevasses in Larsen C ice shelf and implications for their global abundance. *The Cryosphere* **6**, 113–123. doi: 10.5194/tc-6-113-2012

MacAyeal DR, Scambos TA, Hulbe CL and Fahnestock MA (2003) Catastrophic ice-shelf break-up by an ice-shelf-fragment-capsize mechanism. *Journal of Glaciology* **49**(164), 22–36. doi: 10.3189/172756503781830863

MacAyeal DR and Sergienko OV (2013) The flexural dynamics of melting ice shelves. *Annals of Glaciology* **54**(63), 1–10. doi: 10.3189/2013AoG63A256

Malvern LE (1969) *Introduction to the Mechanics of a Continuous Medium*, Englewood Cliffs, NJ: Prentice-Hall

McGrath D and 6 others (2014) The structure and effect of suture zones in the Larsen C ice shelf, antarctica. *Journal of Geophysical Research: Earth Surface* **119**(3), 588–602. doi: 10.1002/2013JF002935

Meng Y, Culberg R and Lai CY (2024) Vulnerability of firn to hydrofracture: poromechanics modeling. *Journal of Glaciology* **70**, e45. doi: 10.1017/jog.2024.47

Meng Y and 6 others (2025) Seasonal changes of mélange thickness coincide with Greenland calving dynamics. *Nature Communications* **16**(1), 573. doi: 10.1038/s41467-024-55241-7

Moore J (1993) Ice blisters and ice dolines. *Journal of Glaciology* **39**(133), 714–716. doi: 10.3189/S002214300001666X

Morlighem M and 6 others (2016) Modeling of Store Gletscher's calving dynamics, west Greenland, in response to ocean thermal forcing. *Geophysical Research Letters* **43**(6), 2659–2666. doi: 10.1002/2016GL067695

Morlighem M and 7 others (2024) The west antarctic ice sheet may not be vulnerable to marine ice cliff instability during the 21st century. *Science Advances* **10**(34), eado7794. doi: 10.1126/sciadv.ado7794

Needell C and Holschuh N (2023) Evaluating the retreat, arrest, and regrowth of crane glacier against marine ice cliff process models. *Geophysical Research Letters* **50**(4), e2022GL102400. doi: 10.1029/2022GL102400

Nekrasov P and MacAyeal DR (2023) Ocean wave blocking by periodic surface rolls fortifies arctic ice shelves. *Journal of Glaciology* **69**(278), 1740–1750. doi: 10.1017/jog.2023.58

Nick F, van der Veen C, Vieli A and Benn D (2010) A physically based calving model applied to marine outlet glaciers and implications for the glacier dynamics. *Journal of Glaciology* **56**(199), 781–794. doi: 10.3189/002214310794457344

Nye JF (1955) Comments on Dr. Loewe's letter and notes on crevasses. *Journal of Glaciology* **2**(17), 512–514. doi: 10.3189/S0022143000032652

Pollard D, DeConto RM and Alley RB (2015) Potential antarctic ice sheet retreat driven by hydrofracturing and ice cliff failure. *Earth and Planetary Science Letters* **412**, 112–121. doi: 10.1016/j.jpgl.2014.12.035

Pralong A and Funk M (2005) Dynamic damage model of crevasse opening and application to glacier calving. *Journal of Geophysical Research: Solid Earth* **110**(B1), B01309. doi: 10.1029/2004JB003104

Rea BR and Evans DJA (2011) An assessment of surge-induced crevassing and the formation of crevasse squeeze ridges. *Journal of Geophysical Research: Earth Surface* **116**(F4), F04005. doi: 10.1029/2011JF001970

Rignot E, Ciracì E, Scheuchl B, Tolpekin V, Wollersheim M and Dow C (2024) Widespread seawater intrusions beneath the grounded ice of Thwaites Glacier, West Antarctica. *Proceedings of the National Academy of Sciences* **121**(22), e2404766121. doi: 10.1073/pnas.2404766121

Robel AA, Wilson E and Seroussi H (2022) Layered seawater intrusion and melt under grounded ice. *The Cryosphere* **16**(2), 451–469. doi: 10.5194/tc-16-451-2022

Rudnicki JW (2014) *Fundamentals of Continuum Mechanics*. New Jersey: John Wiley & Sons.

Sartore NB, Wagner TJW, Siegfried MR, Pujara N and Zoet LK (2025) Wave erosion, frontal bending, and calving at ross ice shelf. *The Cryosphere* **19**(1), 249–265. doi: 10.5194/tc-19-249-2025

https://doi.org/10.1017/jog.2025.10068 Published online by Cambridge University Press

Scambos T and 8 others (2009) Ice shelf disintegration by plate bending and hydro-fracture: Satellite observations and model results of the 2008 Wilkins Ice Shelf break-ups. *Earth and Planetary Science Letters* **280**(1), 51–60. doi: 10.1016/j.jpgl.2008.12.027

Sergienko O (2025) Treatment of the ice-shelf backpressure and buttressing in two horizontal dimensions. *Journal of Glaciology* **71**, e7. doi: 10.1017/jog.2024.83

Slater DA and Wagner TJ (2025) Calving driven by horizontal forces in a revised crevasse-depth framework. *The Cryosphere* **19**(7), 2475–2493.

Slater DA, Nienow PW, Goldberg DN, Cowton TR and Sole AJ (2017) A model for tidewater glacier undercutting by submarine melting. *Geophysical Research Letters* **44**(5), 2360–2368. doi: 10.1002/2016GL072374

Tada H, Paris PC and Irwin GR (2000) *The Stress Analysis of Cracks Handbook, Third Edition*. New York: ASME Press. doi: 10.1115/1.801535

Turcotte D and Schubert G (2014) *Geodynamics*. 3nd Edn. Cambridge: Cambridge University Press. doi: 10.1017/CBO9780511843877

Vallot D and 9 others (2018) Effects of undercutting and sliding on calving: a global approach applied to Kronebreen, Svalbard. *The Cryosphere* **12**(2), 609–625. doi: 10.5194/tc-12-609-2018

van der Veen C (1986) Numerical modelling of ice shelves and ice tongues. *Annales geophysicae. Series B. Terrestrial and Planetary physics* **4**(1), 45–53

van der Veen C (1998a) Fracture mechanics approach to penetration of bottom crevasses on glaciers. *Cold Regions Science and Technology* **27**(3), 213–223. doi: 10.1016/S0165-232X(98)00006-8

van der Veen C (1998b) Fracture mechanics approach to penetration of surface crevasses on glaciers. *Cold Regions Science and Technology* **27**(1), 31–47. doi: 10.1016/S0165-232X(97)00022-0

van der Veen C and Whillans I (1989) Force budget: I. Theory and numerical methods. *Journal of Glaciology* **35**(119), 53–60. doi: 10.3189/002214389793701581

Wagner TJW, James TD, Murray T and Vella D (2016) On the role of buoyant flexure in glacier calving. *Geophysical Research Letters* **43**(1), 232–240A. doi: 10.1002/2015GL067247

Wagner TJW and 8 others (2014) The "footloose" mechanism: Iceberg decay from hydrostatic stresses. *Geophysical Research Letters* **41**(15), 5522–5529. doi: 10.1002/2014GL060832

Weertman J (*1896-1977*) Theory of water-filled crevasses in glaciers applied to vertical magma transport beneath oceanic ridges. *Journal of Geophysical Research* **76**(5), 1171–1183. doi: 10.1029/JB076i005p01171

Weertman J (1957) Deformation of floating ice shelves. *Journal of Glaciology* **3**(21), 38–42. doi: 10.3189/S0022143000024710

Wells-Moran S, Ranganathan M and Minchew B (2025) Fracture criteria and tensile strength for natural glacier ice calibrated from remote sensing observations of antarctic ice shelves. *Journal of Glaciology* **71**(11), e47. doi: 10.1017/jog.2024.104

Wilner JA, Morlighem M and Cheng G (2023) Evaluation of four calving laws for antarctic ice shelves. *The Cryosphere* **17**(11), 4889–4901. doi: 10.5194/tc-17-4889-2023

Wilson EA, Wells AJ, Hewitt IJ and Cenedese C (2020) The dynamics of a subglacial salt wedge. *Journal of Fluid Mechanics* **895**, A20. doi: 10.1017/jfm.2020.308

Xie S, Dixon TH, Holland DM, Voytenko D and Vaňková I (2019) Rapid iceberg calving following removal of tightly packed pro-glacial mélange. *Nature Communications* **10**(1), 3250. doi: 10.1038/s41467-019-10908-4

Yu H, Rignot E, Morlighem M and Seroussi H (2017) Iceberg calving of Thwaites Glacier, West Antarctica: full-Stokes modeling combined with linear elastic fracture mechanics. *The Cryosphere* **11**(3), 1283–1296. doi: 10.5194/tc-11-1283-2017

Zarrinderakht M, Schoof C and Peirce A (2022) The effect of hydrology and crevasse wall contact on calving. *The Cryosphere* **16**(10), 4491–4512. doi: 10.5194/tc-16-4491-2022

Zarrinderakht M, Schoof C and Peirce A (2024) An analysis of the interaction between surface and basal crevasses in ice shelves. *The Cryosphere* **18**(8), 3841–3856. doi: 10.5194/tc-18-3841-2024

Zarrinderakht M, Schoof C and Zwinger T (2023) A leading-order viscoelastic model for crevasse propagation and calving in ice shelves. *EGUsphere* **2023**, 1–35. doi: 10.5194/egusphere-2023-807

Zhang E, Catania G and Trugman DT (2023) Autoterm: an automated pipeline for glacier terminus extraction using machine learning and a "big data" repository of Greenland glacier termini. *The Cryosphere* **17**(8), 3485–3503. doi: 10.5194/tc-17-3485-2023

Appendix A. Crack Depth d/H versus Dimensionless Water Level λ

In this Appendix, we seek to further develop intuition for the HFB theory, specifically for crack depths as functions of the dimensionless water level λ, buttressing B and the dimensionless surface crevasse meltwater depth $\tilde{h}_w$. Figure 9a represents a calving regime diagram as a function of dimensionless water level versus buttressing. Choosing one crack configuration, one may select a point on this calving regime diagram and have a corresponding measure of crack depths. In Fig. 8, we examine horizontal slices, or fixed values of dimensionless water level λ, of Fig. 9a for a dry surface crevasse atop a saltwater basal crevasse (DS+SB). In this appendix, we consider vertical slices, or fixed dimensionless buttressing B, of Fig. 9a with variable surface meltwater $\tilde{h}_w \equiv h_w/H$ as plotted in Fig. A1.

In Fig. A1, a surface crevasse without a basal crevasse on a MTG would have depth $d_s^\natural$. If basal crevasses form, the surface crevasse associated with this dual fracture setup d_s branches slightly off from this surface-crevasse-only curve, and may enable calving.

The first row, a and b, represent vertical transects of Fig. 9a at $B = 0.15$ and $B = 0.3$, respectively. We see in b that by increasing the buttressing, we shut off the low-pressure meltwater basal crevasses (DS+LMB in blue shading in a) from forming, as there is not enough tension. Furthermore, the dimensionless water level required for calving from a high pressure meltwater basal crevasse (DS+HMB in dash-dotted black) decreases, while the calving threshold for a saltwater basal crevasse (DS+SB in dash-dotted purple) does not change. Thus, lowering ocean water level *stabilizes* a saltwater basal crevasse yet *destabilizes* a meltwater basal crevasse.

Comparing each row, we see minimal change between dry surface crevasses (DS) from a to b and surface crevasses with meltwater (MS) filling 10% of the ice thickness from c to d. However, comparing e to f where meltwater fills 50% of the ice thickness, we see a large change for surface crevasses with meltwater (MS). By increasing the amount of water relative to the ice thickness $\tilde{h}_w \equiv h_w/H$, we see calving around $\lambda \sim 0.4$. Furthermore, the meltwater-surface-crevasse-alone crack depth $d_s^\natural$ is typically greater in e than in f, and all other crack configurations branch from this solution. Thus, whereas in b there is not enough tension for a low-pressure meltwater basal crevasse (DS+LMB in blue) to form, in e this configuration cannot form because the meltwater-containing surface crevasse has already calved at a higher dimensionless water level.

We end with two subtle points related to crack formation (dashed lines) and calving thresholds (dashed-dotted lines) for meltwater and saltwater basal crevasses. First, akin to how smaller head height z_h results in a smaller window for meltwater basal crevasses (DS+MB) to exist in Fig. 9a, we see the same behavior in (MS+MB) by increasing surface meltwater $\tilde{h}_w$ comparing each row of Fig. A1. However, this is purely due to a change in the crack formation threshold B^F; the calving threshold B^* does not change. On the other hand, for surface crevasses atop saltwater basal crevasses (MS+SB), both crack formation B^F and calving B^* thresholds change with $\tilde{h}_w$, requiring higher dimensionless water level λ and thus higher saltwater pressure for the crack to form B^F, and less pressure for calving B^*. Importantly, with a dry surface crevasse and saltwater basal crevasse (DS+SB), the critical dimensionless water level λ for calving remains above 1, which represents flotation. Scenarios with $\lambda > 1$, and thus calving by saltwater basal crevasse in these panels, represent an unlikely super-buoyant case (Benn and others, 2017).

Appendix B. Torque Equilibrium Calving Argument

Recent work has established that the stress required for calving from a one horizontal dimension ice shelf basal crevasse may be described through a torque-balance argument (Zarrinderakht and others, 2022). This torque-balance argument matches with the result of LEFM (van der Veen, 1998a, Tada and others, 2000, Lai and others, 2020). Additionally, this torque balance has been used

https://doi.org/10.1017/jog.2025.10068 Published online by Cambridge University Press

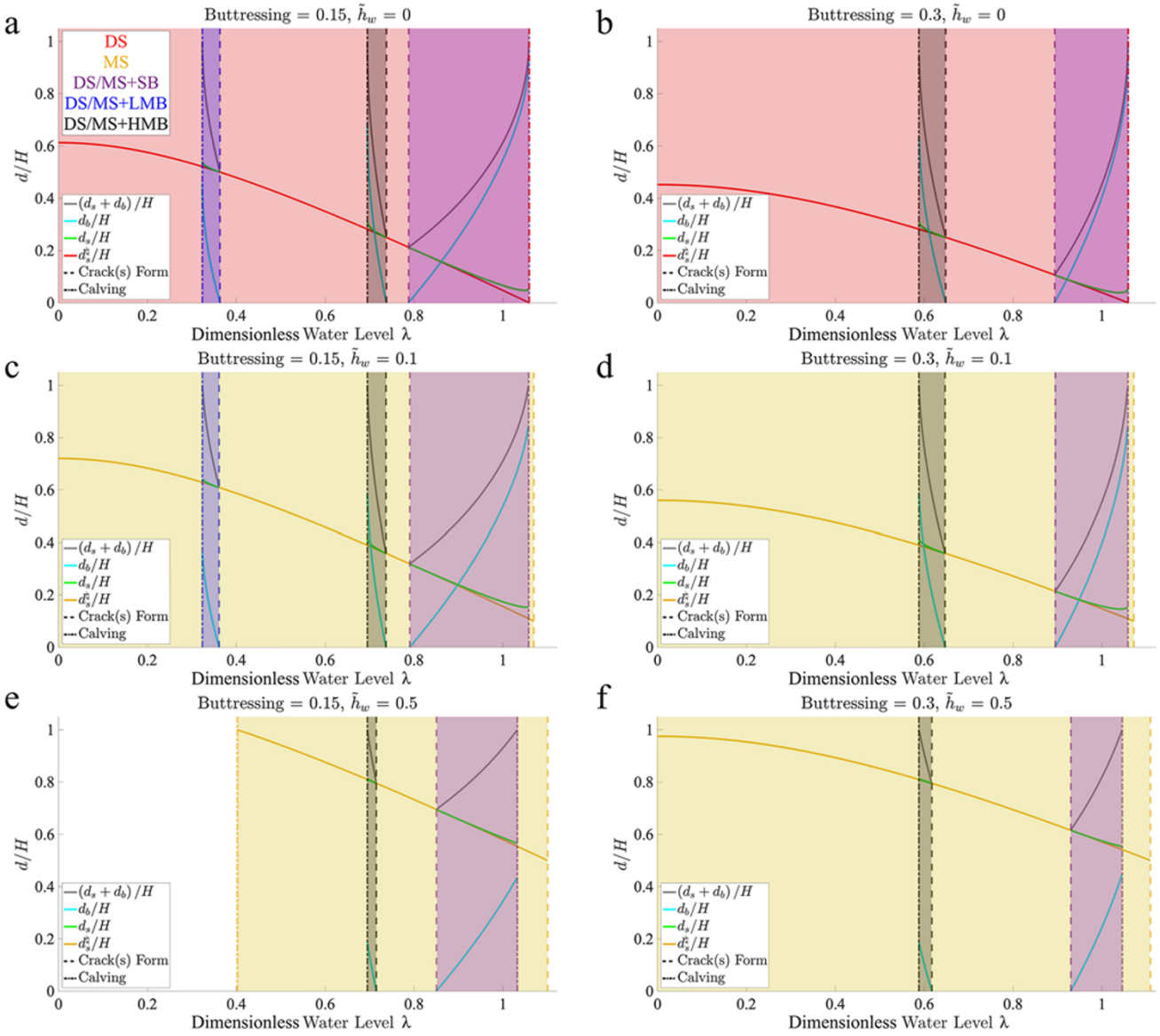

Figure A1. Transects of the dimensionless water level and buttressing calving regime diagram of Figure 9a, with dimensionless crack depths versus water level given buttressing. The left column a, c and e use a buttressing value of $B = 0.15$, while the right column b, d and f use $B = 0.3$. The first row, a and b, have dry surface crevasses $\tilde{h}_w \equiv h_w/H = 0$, while the second and third rows, c, d and e, f, have surface crevasses with meltwater to fill 10% or 50% of the ice thickness, respectively. Shaded contours represent where crack configuration solutions (DS, MS, DS/MS+SB, DS/MS+LMB, DS/MS+HMB) exist. We use a similar crack configuration color key as Figure 9a.

to approximately describe the calving stress in Mode I basal crevasse LEFM including a vertical temperature profile (Coffey and others, 2024). However, as noted in Yu and others (2017), Jiménez and Duddu (2018), Zarrinderakht and others (2022), Coffey and others (2024), an issue with this formulation is that the ice shelf base is treated as stress-free. Instead, a hydrostatic ocean would exert pressure on the ice base as it deforms and would affect the stress required for calving. Including this pressure in our torque balance, we show that the only rifting stress that can satisfy both force balance and torque balance with beam flexure explicitly modeled is $\overline{R}_{xx} = \frac{1}{2}(1 - \rho_i/\rho_w)\rho_i g H$ or $B^* = 0$, the HFB result.

In static equilibrium, where forces and torques sum to zero, the relevant component of torque τ_y at the crevassed location $x = x_c$ may be written as

$$\tau_y = (\underline{r} \wedge \underline{F}) \cdot \underline{\hat{y}} = r_z F_x - r_x F_z = 0, \tag{B.1}$$

where following Zarrinderakht and others (2022), we take $\underline{r}$ to be the distance vector from the crevassed location at the surface $(x = x_c, z = s)$, $\underline{F}$ is the force vector, $\underline{\hat{y}}$ is the unit vector into the page, and r_x, r_z and F_x, F_z are the distances and forces in the horizontal and vertical, respectively. The first term, $r_z F_x$, is included in Zarrinderakht and others (2022), Coffey and others (2024), and accounts for the forces acting along the newly-formed rift walls. The second term, $-r_x F_z$, is missing from previous work, and accounts for the hydrostatic restoring force of the ocean due to ice shelf base vertical displacement. Thus, the torque is not balanced purely at the rift location $x = x_c$, but instead is balanced some length in x of the ice shelf or newly-formed iceberg.

In the case where the ice shelf can be modeled as incompressible, (B.1) may be written as

$$2\left[\int_b^s (R_{xx} - \rho_i g\,(s - z))\,(s - z)\,dz + \int_b^0 \rho_w g z\,(s - z)\,dz\right] - 2\rho_w g \int_0^L w\,(x)\,x dx = 0. \tag{B.2}$$

https://doi.org/10.1017/jog.2025.10068 Published online by Cambridge University Press

The first two terms come from $r_z F_x$ and are the torques acting along the newly-formed rift walls, while the last term comes from $-r_x F_z$ and is the force applied along the deflecting ice shelf base, with $w(x) > 0$ indicating downward ice shelf deflection (Turcotte and Schubert, 2014). This configuration considers the basal crack x_c to be in the center of a symmetric ice shelf of length $2L$.

The rifting stress can be obtained by solving (B.2) for $\overline{R}_{xx}$. This has been done in Zarrinderakht and others (2022), Coffey and others (2024), neglecting the last term in (B.2) due to the ocean restoring force,

$$\frac{\overline{R}_{xx}}{\frac{1}{2}\left(1-\frac{\rho_i}{\rho_w}\right)\rho_i g H} = \frac{2}{3}\left(2-\frac{\rho_i}{\rho_w}\right). \tag{B.3}$$

However, this rifting stress ignoring ocean restoring force is inconsistent with the rifting stress obtained from HFB $\overline{R}_{xx} = \overline{R}_{xx}^{IT} \equiv \frac{1}{2}\left(1-\frac{\rho_i}{\rho_w}\right)\rho_i g H$. Below we show how by considering the ocean restoring force (the last term in (B.2)), the torque balance would not be inconsistent with the HFB.

If we model ice as a thin elastic beam (Hetényi and Hetbenyi, 1946, Turcotte and Schubert, 2014), which inherently assumes force balance in the calculation of deflection $w(x)$ with the bending moment at the crevassed location $M_c \equiv M(x = x_c)$, we will converge to the same answer as HFB theory but with the addition of explicitly modeling bending. From Hetényi and Hetbenyi (1946), Turcotte and Schubert (2014), the deflection profile is akin to the bending of the elastic lithosphere at an ocean trench (Turcotte and Schubert, 2014). With $x = 0$ placed at rift location, the deflection may be written as

$$w(x) = \frac{\alpha^2 M_c}{2D}\exp\left(\frac{-x}{\alpha}\right)\left(\left(\frac{V_c\alpha}{M_c}+1\right)\cos\frac{x}{\alpha} - \sin\frac{x}{\alpha}\right), \tag{B.4}$$

with the flexural wavelength

$$\alpha \equiv \left[\frac{4D}{\rho_w g}\right]^{1/4}, \tag{B.5}$$

where V_c is the shear force and $D = EH^3/\left(12\left(1-\nu^2\right)\right)$ is the rigidity. Unlike the lithosphere problem in Turcotte and Schubert 2014, there is no shear force applied to the beam surface that pushes the beam downward/upward so $V_c = 0$. Thus, evaluating (B.2) with (B.4) and (B.5), and taking the limit as the length of the ice shelf L approaches infinity,

$$\lim_{L\to\infty}\int_0^L w(x)\,x dx = -\frac{\alpha^2}{2}\frac{\alpha^2 M_c}{2D} = -\frac{M_c}{\rho_w g}, \tag{B.6}$$

and we may write the torque along the ice shelf base as

$$-r_x F_z = 2M_c. \tag{B.7}$$

Substituting (B.7) into (B.2) we have

$$2\left[\int_b^s \left(R_{xx} - \rho_i g\left(s-z\right)\right)\left(s-z\right)dz + \int_b^0 \rho_w g z\left(s-z\right)dz\right] - 2M_c = 0, \tag{B.8}$$

with bending moment

$$M_c = \int_b^s \left(R_{xx} - \rho_i g\left(s-z\right)\right)\left(s-z\right)dz + \int_b^0 \rho_w g z\left(s-z\right)dz. \tag{B.9}$$

This bending moment has been defined in previous literature (e.g. Weertman (1957), Buck (2024)) with a different $z = 0$; however, this does not change the final expression. What is important is the moment arm (the vertical distance from the ice surface in this problem $(s-z)$) is the same as that used in Zarrinderakht and others (2022) and in the bracket term in (B.8). Therefore, the torque-balance constraint cannot be used to solve for the depth-averaged rifting stress $\overline{R}_{xx}$ when the ice shelf base can deflect, as used (Zarrinderakht and others, 2022, Coffey and others, 2024) to describe rifting from basal crevasse LEFM (van der Veen, 1998a).

Instead, Euler-Bernoulli beam theory inherently assumes static equilibrium, or force and torque balance (Turcotte and Schubert, 2014). As such, the HFB rifting stress, $\overline{R}_{xx} = \frac{1}{2}\left(1-\rho_i/\rho_w\right)\rho_i g H$ or $B^* = 0$, is the unique rifting stress that can satisfy force and torque balance. This helps explain the agreement of HFB with the numerical simulation of basal crevasse rifting with flexure in the blue curves of Fig. 6 in Buck (2023). Additionally, it is clear that a vertical temperature profile would not modify this result, providing a simple explanation for the result of Coffey and others (2024) that the rifting stress threshold with HFB is independent of the vertical temperature profile.

Appendix C. Model Limitations

C.1. Material strength and energy

One potential limitation of our HFB model may be the lack of a material strength or fracture toughness (Lawn, 1993, Litwin and others, 2012). We develop a scaling argument that suggests that the added force required to overcome the material strength through the entire ice thickness is negligible compared to the force required to calve a glacier with zero fracture toughness.

One way to envision the zero material strength assumption in HFB is to consider a row of touching domino tiles. There is no cohesive force between each tile and its neighbor; thus, at each tile border, there is zero strength. The force required for full separation of tiles, i.e. calving, may be written considering conservative forces only as

$$F_x = \frac{\partial U}{\partial x}, \tag{C.1}$$

where in the absence of a fracture toughness or other sources of potential energy, the potential energy is just gravitational, $U = U_G$. This has already been shown to describe the HFB theory (Coffey and others, 2024) and compressive buckling (Coffey and others, 2022). In fracture mechanics (Lawn, 1993, Anderson, 2017), the Griffith criterion for crack growth is

$$\frac{\partial \mathcal{U}}{\partial C} = 0, \tag{C.2}$$

where $\mathcal{U}$ is the total energy of the system, and C is crack length times length into the page (Lawn, 1993, Anderson, 2017). Following Lawn 1993, a nonzero material strength (thus nonzero fracture toughness) may be defined with a surface energy U_S. The surface energy release rate may be written as

$$\frac{\partial U_S}{\partial C} = \frac{K_{Ic}^2}{E'}, \tag{C.3}$$

where K_{Ic} is the mode I fracture toughness of ice, measured as 0.15 MPa $\cdot$ m$^{\frac{1}{2}}$ (Litwin and others, 2012), and E' is the Young's Modulus E in plane stress, or $E/\left(1-\nu^2\right)$ in plane strain with Poisson's ratio ν. To have calving, one would need to have $\frac{\partial}{\partial C}\left(U_G + U_I + W_{ext}\right) \geqslant -\frac{\partial U_S}{\partial C}$ for C increasing from initial flaw size through the full thickness, with internal energy U_I, such as elastic strain energy, heat, or chemical effects and external work W_{ext}. We have tacitly assumed kinetic energy is negligible. If there was a nonzero fracture toughness $K_{Ic} > 0$, what would be the force required to overcome this surface energy?

$$F_x = \frac{\partial}{\partial x}\int \frac{\partial U_S}{\partial C}dC = \frac{\partial}{\partial x}\int \frac{K_{Ic}^2}{E'}dC \sim \frac{K_{Ic}^2 H\Delta y}{E'\Delta x}. \tag{C.4}$$

For a saltwater basal crevasse and a dry surface crevasse, the force required to calve with zero fracture toughness is

$$F_x = \frac{\partial U_G}{\partial x} = \frac{\Delta y}{2}\left(1-\frac{\rho_i}{\rho_w}\lambda^2\right)\rho_i g H^2. \tag{C.5}$$

The ratio of these forces gives,

$$\frac{2K_{Ic}^2}{E'\Delta x\left(1-\frac{\rho_i}{\rho_w}\lambda^2\right)\rho_i g H} \sim O\left(10^{-6}\right), \tag{C.6}$$

where we have taken fracture toughness as above, $E' \sim 10^9$ Pa, $\Delta x = 100$ m, $\rho_i = 917$ kg m^{-3}, $\rho_w = 1028$ kg m^{-3}, $g = 9.8$ m s^{-2}, $H = 300$ m, and $\lambda = 1$. The surface energy U_S term (related to material strength) in Griffith's energy balance $\frac{\partial}{\partial C}\left(U_G + U_I + W_{ext}\right) \geqslant -\frac{\partial U_S}{\partial C}$ is negligible compared with the gravitational potential term U_G. Thus, our simple scaling argument suggests that the force required to calve a glacier with zero fracture toughness, in the absence of buttressing, is approximately the same as that of a glacier with the fracture toughness of ice (Litwin and others, 2012).

https://doi.org/10.1017/jog.2025.10068 Published online by Cambridge University Press

C.2. Alternate mechanisms

In this section, we summarize the alternate mechanisms that we do not consider in this paper. Our force balance predicts tensile hydrofracture-induced calving involves full-thickness fracture. However, as suggested by Weertman and others (Weertman, 1971, Zarrinderakht and others, 2022), the closure of surface crevasse tips may also enable drainage and hydrofracture without necessarily causing calving.

Second, we do not model the non-isostatic effects of lake loading, drainage, flexural unloading, nor calving aftereffects (MacAyeal and others, 2003, Scambos and others, 2009, Amundson and others, 2010, Banwell and others, 2013, MacAyeal and Sergienko, 2013). Dolines, moulins and blisters underneath the ice sheet (Moore, 1993, Chase and others, 2021, Lai and others, 2021, Banwell and others, 2024, Hageman and others, 2024) are consequences of lake loading and drainage on ISs and ice sheets. The nearly axisymmetric nature of these drainage features suggests that a full 3D stress field may be required to model drainage that can lead to calving (Banwell and others, 2013, MacAyeal and Sergienko, 2013).

Tides and ocean waves can also elastically deform the ice and induce stresses that interact with crevasses (Freed-Brown and others, 2012, Nekrasov and MacAyeal, 2023). While we do not model these time-dependent processes, if we allow for thin beam flexure, we show in Appendix B that a torque-balance argument will converge to our $B^* = 0$ solution.

C.3. Constant density

We assume constant densities for both the ice and the water source. We note that firn has been implicated as important for surface crevasses (Gao and others, 2023, Clayton and others, 2024, Meng and others, 2024). We leave $\rho(z)$ effects as an area of possible future study.

C.4. Thermomechanical effects

If coupling force balance with the heat equation, one could potentially consider crevasse wall refreezing or melting. Future work fully accounting for these time-dependent thermomechanical processes may yield insightful results.

C.5. Complicated or unknown fracture processes

There are many possible complications with fracture mechanics and rheology (Zarrinderakht and others, 2023), such as stress concentration, the fracture process zone length (Pralong and Funk, 2005), material behavior (brittle, quasibrittle, or ductile) and a potential size effect (Bažant and others, 2021), crack tip shielding (Zarrinderakht and others, 2024), crack nucleation given ice fabric and deformation mechanism (Frost, 2001), flexure, shear (Clerc and others, 2019, Bassis and others, 2021, Needell and Holschuh, 2023) and densely spaced fractures.

An assumption of HFB is that changes in traction applied to our ice geometry (Fig. 2) must be balanced by crack-depth changes. In reality, the rheology of ice permits internal viscous deformation that can accommodate changing boundary conditions.

Appendix D. Deriving Buttressing from van der Veen and Whillans' Force Balance

The goal of this Appendix is twofold. First, we find the common form of buttressing in (10), as shown for ISs in Gudmundsson (2013). We show the assumptions that are required for ISs, marine- and land-terminating glaciers to arrive at (10). We assume constant thickness and flat bed slope for MTGs, and flat bed slope for LTGs. Second, we discuss extending the force balance to 3D. We conclude by discussing a challenge of applying HFB in 3D.

Depth-integrating the Stokes equations and using a traction-free surface boundary condition, the $\hat{x}$-component of the momentum equation was derived in Van Der Veen and Whillans 1989 (see equation 14):

$$\partial_x \int_b^s R_{xx} dz + \partial_y \int_b^s R_{xy} dz - \rho_i g H \partial_x s - R_{xz}|_{(z=b)} + R_{xx}|_{(z=b)} \partial_x b + R_{yx}|_{(z=b)} \partial_y b = 0. \quad \text{(D.1)}$$

Following the convention set in Cuffey and Paterson 2010, we will denote the second term as $-\tau_w$, and group the last 3 terms as the total basal resistance $-\tau_{bx}$. To turn this equation into a force-balance equation per unit width, we integrate the above equation from x_c to x_t and use $H = s - b$,

$$H\overline{R}_{xx}|_{x_c}^{x_t} - \int_{x_c}^{x_t} (\tau_w + \tau_{bx})\, dx - \rho_i g \left(\frac{H^2}{2}\Big|_{x_c}^{x_t} + \int_{x_c}^{x_t} H \partial_x b dx \right) = 0. \quad \text{(D.2)}$$

For our local force-balance argument, the quantity of interest at x_c is $\int_b^s \sigma_{xx} dz$. We may rearrange to solve for this,

$$\int_b^s \sigma_{xx}|^{x_c} dz = H\overline{R}_{xx}|^{x_c} - \frac{\rho_i g}{2} H^2|^{x_c} = H\overline{R}_{xx}|^{x_t} - \frac{\rho_i g}{2} H^2|^{x_t} - \int_{x_c}^{x_t} (\tau_w + \tau_{bx})\, dx - \rho_i g \int_{x_c}^{x_t} H \partial_x b dx. \quad \text{(D.3)}$$

We focus here on the last two terms on the right-hand side: 1) gradients in the depth-integrated horizontal shear stresses due to the lateral wall τ_w and the basal drag τ_{bx}, and 2) the basal topography-induced stress. Given constant thickness, retrograde bed slope provides a force in the opposite direction of the flow, and vice versa. Typically, we expect τ_w and τ_{bx} to greatly contribute to normal buttressing, as these forces originate from drag applied at the lateral and bottom boundaries of the glacier.

D.1. Ice shelf buttressing

For ISs, the horizontal component of normal stress along the base $\rho_i g H \partial_x b$ can be calculated using the isostatic assumption $b = -\frac{\rho_i}{\rho_w} H$. The horizontal force per unit width at x_c becomes

$$\int_b^s \sigma_{xx}|^{x_c} dz = \int_b^s \sigma_{xx}|^{x_t} dz - \int_{x_c}^{x_t} (\tau_w + \tau_{bx})\, dx + \rho_i g \int_{x_c}^{x_t} \frac{\rho_i}{\rho_w} H \partial_x H dx \quad \text{(D.4a)}$$

$$= \int_b^s \left[R_{xx} - \rho_i g\,(s - z) \right]^{x_t} dz - \int_{x_c}^{x_t} (\tau_w + \tau_{bx})\, dx + \rho_i g \frac{\rho_i}{\rho_w} \frac{H^2}{2}\Big|_{x_c}^{x_t} \quad \text{(D.4b)}$$

$$= H_t \overline{R}_{xx} - \frac{1}{2}\rho_i g H_t^2 - \int_{x_c}^{x_t} (\tau_w + \tau_{bx})\, dx + \rho_i g \frac{\rho_i}{\rho_w} \frac{H^2}{2}\Big|_{x_c}^{x_t} \quad \text{(D.4c)}$$

$$= H_t \overline{R}_{xx}^{B=0} - \left(B_{Mélange}\right) \frac{1}{2} \left(1 - \frac{\rho_i}{\rho_w}\right) \rho_i g H_c^2 - \frac{1}{2}\rho_i g H_t^2 - \int_{x_c}^{x_t} (\tau_w + \tau_{bx})\, dx + \rho_i g \frac{\rho_i}{\rho_w} \frac{H^2}{2}\Big|_{x_c}^{x_t} \quad \text{(D.4d)}$$

$$= \frac{1}{2} \left(1 - \frac{\rho_i}{\rho_w}\right) \rho_i g H_t^2 - \left(B_{Mélange}\right) \frac{1}{2} \left(1 - \frac{\rho_i}{\rho_w}\right) \rho_i g H_c^2 - \frac{1}{2}\rho_i g H_t^2 - \int_{x_c}^{x_t} (\tau_w + \tau_{bx})\, dx + \rho_i g \frac{\rho_i}{\rho_w} \frac{H^2}{2}\Big|_{x_c}^{x_t} \quad \text{(D.4e)}$$

$$= \frac{1}{2} \left(-\frac{\rho_i}{\rho_w}\right) \rho_i g H_c^2 - \left(B_{Mélange}\right) \frac{1}{2} \left(1 - \frac{\rho_i}{\rho_w}\right) \rho_i g H_c^2 - \int_{x_c}^{x_t} (\tau_w + \tau_{bx})\, dx, \quad \text{(D.4f)}$$

where H_t and H_c are the ice thickness at x_t and x_c, respectively. In the transition from (D.4c) to (D.4d), if there is no ice mélange, then $B_{Mélange} = 0$. We

https://doi.org/10.1017/jog.2025.10068 Published online by Cambridge University Press

can write the left-hand side of the equation in terms of $\sigma_{xx} = R_{xx} - \rho_i g(s-z)$ and rearrange (D.4f),

$$H_c \overline{R}_{xx}|^{x_c} = \frac{1}{2}\left(1-\frac{\rho_i}{\rho_w}\right)\rho_i g H_c^2 - \left(B_{Mélange}\right)\frac{1}{2}\left(1-\frac{\rho_i}{\rho_w}\right)\rho_i g H_c^2 - \int_{x_c}^{x_t}\left(\tau_w+\tau_{bx}\right)dx. \tag{D.5}$$

We define the dimensionless buttressing force as

$$B \equiv B_{Mélange} + \frac{\int_{x_c}^{x_t}\left(\tau_w+\tau_{bx}\right)dx}{\frac{1}{2}\left(1-\frac{\rho_i}{\rho_w}\right)\rho_i g H_c^2}, \tag{D.6}$$

such that (D.5) can be written as

$$\frac{\overline{R}_{xx}|^{x_c}}{\frac{1}{2}\left(1-\frac{\rho_i}{\rho_w}\right)\rho_i g H_c} = 1 - B. \tag{D.7}$$

If there is no drag applied to the ice shelf base or lateral margins, then $B = 0$; if there is buttressing then $B > 0$.

D.2. Marine-terminating glacier buttressing

For MTGs and LTGs, the assumption of local isostasy is modified due to the bedrock. Rearranging (D.3), we have that

$$\frac{\overline{R}_{xx}|^{x_c}}{\frac{1}{2}\left(1-\lambda^2\frac{\rho_i}{\rho_w}\right)\rho_i g H_c} = \frac{H_t \overline{R}_{xx}|^{x_t} - \frac{\rho_i g}{2}H^2|_{x_c}^{x_t} - \int_{x_c}^{x_t}\left(\tau_w+\tau_{bx}\right)dx - \rho_i g\int_{x_c}^{x_t} H\partial_x b dx}{\frac{1}{2}\left(1-\lambda^2\frac{\rho_i}{\rho_w}\right)\rho_i g H_c^2}, \tag{D.8}$$

where $\lambda = -\frac{\rho_w}{\rho_i}\frac{b}{H}|^{x_c}$ is the dimensionless water level. To achieve consistency with the ice shelf case, we can simplify the MTG case to have a constant thickness and a flat bed. This allows (D.8) to be written as

$$\frac{\overline{R}_{xx}|^{x_c}}{\frac{1}{2}\left(1-\lambda^2\frac{\rho_i}{\rho_w}\right)\rho_i g H_c} = -B_{Mélange} + \frac{\frac{1}{2}\left(1-\lambda^2\frac{\rho_i}{\rho_w}\right)\rho_i g H_c^2 - 0 - \int_{x_c}^{x_t}\left(\tau_w+\tau_{bx}\right)dx - 0}{\frac{1}{2}\left(1-\lambda^2\frac{\rho_i}{\rho_w}\right)\rho_i g H_c^2}. \tag{D.9}$$

Thus, the buttressing number for the constant thickness and flat bed MTG is defined as

$$B \equiv 1 - \frac{\overline{R}_{xx}|^{x_c}}{\frac{1}{2}\left(1-\lambda^2\frac{\rho_i}{\rho_w}\right)\rho_i g H_c} = B_{Mélange} + \frac{\int_{x_c}^{x_t}\left(\tau_w+\tau_{bx}\right)dx}{\frac{1}{2}\left(1-\lambda^2\frac{\rho_i}{\rho_w}\right)\rho_i g H_c^2}, \tag{D.10}$$

Following Meng and others (2025), a simple form for the dimensionless mélange buttressing force per unit width is

$$B_{Mélange}(t) = \left[\frac{1}{2}\left(1-\frac{\rho_i}{\rho_w}\right)\phi\rho_i g H_M^2(t)\right] / \left[\frac{1}{2}\left(1-\lambda^2\frac{\rho_i}{\rho_w}\right)\rho_i g H_c\right] = \phi\left(\frac{H_M(t)}{H_c}\right)^2 \frac{1-\frac{\rho_i}{\rho_w}}{1-\frac{\rho_i}{\rho_w}\lambda^2}, \tag{D.11}$$

with mélange porosity ϕ and seasonally-varying mélange thickness $H_M(t)$.

D.3. Land-terminating glacier buttressing

For LTGs, there is no mélange at the ice front. Force balance at the ice front guarantees that $H_t \overline{R}_{xx}|^{x_t} - \frac{\rho_i g}{2}H_t^2 = 0$. Thus, (D.8) simplifies to

$$\frac{\overline{R}_{xx}|^{x_c}}{\frac{1}{2}\rho_i g H_c} = 1 - \frac{\int_{x_c}^{x_t}\left(\tau_w+\tau_{bx}+\rho_i g H\partial_x b\right)dx}{\frac{1}{2}\rho_i g H_c^2} = 1 - B. \tag{D.12}$$

To achieve consistency with the MTG definition of the buttressing number (D.10), we assume a flat bed. For the MTG result to converge to the LTG result, the LTG must have constant thickness; similarly, the MTG result converges to the IS case when the IS has a flat ice shelf bed elevation b.

D.4. 3D force balance

Our HFB analysis can be extended to 3 spatial dimensions, which is not included in the paper, but would involve one more integral along y of (D.3). One should account for variable bed slope and thickness, yielding

$$\int_{y_L}^{y_R}\int_b^s \sigma_{xx}|^{x_c} dz dy = \int_{y_L}^{y_R}\left[H\overline{R}_{xx}|^{x_t} - \frac{\rho_i g}{2}H^2|^{x_t} - \int_{x_c}^{x_t}\left(\tau_{bx}+\rho_i g H\partial_x b\right)dx\right]dy + \int_{x_c}^{x_t} H\overline{R}_{xy}|_{y_L}^{y_R} dx. \tag{D.13}$$

If we had an arbitrary shape, we would use (3) and arrive at the same conclusion: the horizontal forces acting on the control volume must balance.

In the application of HFB to more complicated geometries, one must determine the control volume, which may potentially align with a curved crevasse plane and may not be a priori known. This may be an interesting avenue for future research.

https://doi.org/10.1017/jog.2025.10068 Published online by Cambridge University Press